

On-board antennas reference design for the STM32WB Series MCUs

Introduction

This document describes the design, fabrication, and radio electrical characterization (S11 parameter and radiation) of a set of seven antennas associated with their electronic board, operating on the ISM 2.45 GHz frequency band and available for the STM32WB Series microcontrollers.

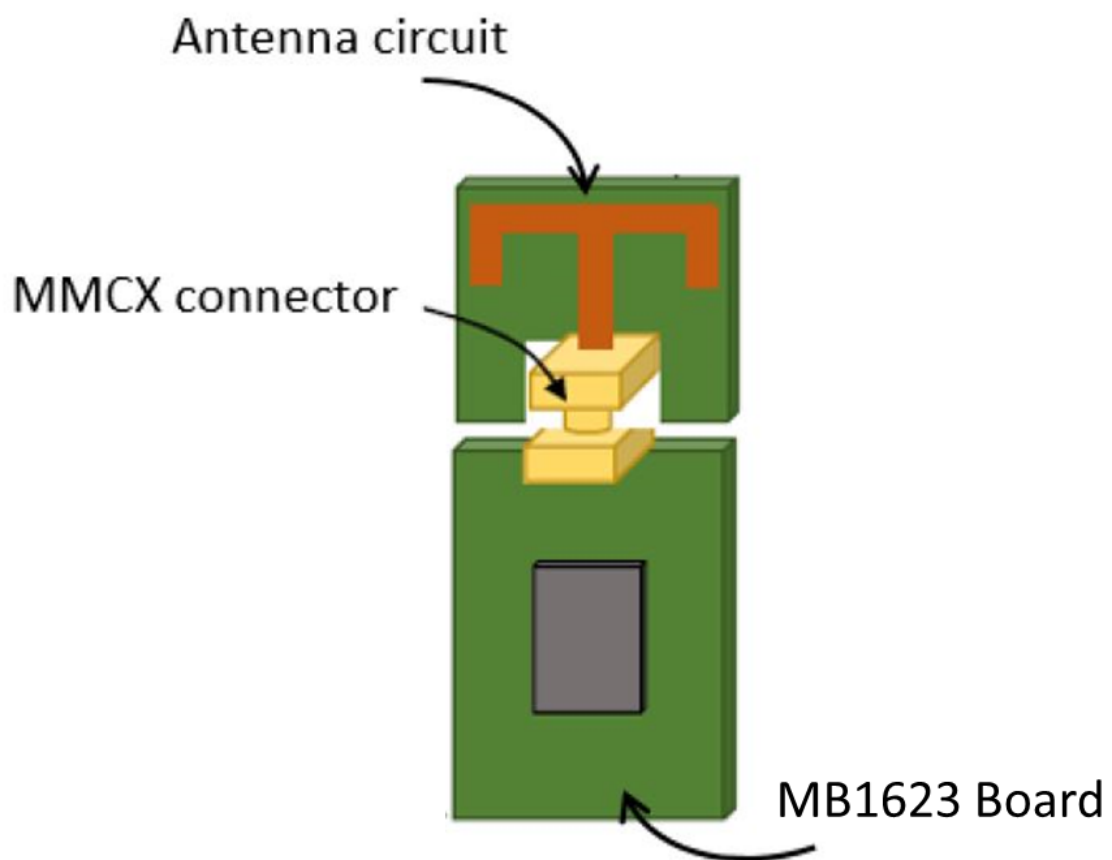
The seven antenna types are:

- Monopole T-shaped antenna
- Monopole L-shaped antenna
- Inverted F Antenna – IFA
- Microstrip meandered monopole antenna
- IFA metal plane antenna
- Yagi-Uda antenna
- Chip antenna

1 Reference board

These antennas are benchmarked with the MB1623 board, equipped with an Arm® Cortex®-based microcontroller. This board is 40 mm high and 30 mm wide, and the connector is centered along the width at the top, as shown in [Figure 1](#). Considering the limited dimensions compared to the operating wavelength, as well as the MB1623 board orientation that can adjust the antenna radiation properties, the proximity of the board must be taken into consideration during the design process.

[Figure 1. Reference board](#)



Design and manufacturing

The following section focuses on the design and fabrication of the antennas. In each sub-section, the simulated radio-electrical performances of each antenna type are presented. In addition, a section is dedicated to the fabrication of the antenna prototypes.

Note:

Arm is a registered trademark of Arm Limited (or its subsidiaries) in the US and/or elsewhere.

arm

2 Context

From a design point of view, the proposed structures must respect different requirements including the size that must not exceed 100x50 mm². The antenna is etched on an FR4 substrate that is 1.6 mm thick.

The required radiation performances can be summarized as follow:

- Operating frequency band: from 2.402 to 2.480 GHz
- Reflection coefficient: -9.54 dB
- Radiation efficiency: 50 %

The simulation of the radio electrical performances of the different antennas is achieved using two different electromagnetic software simulations, CST Microwave Studio and ANSYS HFSS. The antenna radiation behavior is simulated in its real operating context and optimized to match the desired radio-electrical requirements. The simulation results of each optimized design following an antenna geometry tuning is presented and analyzed in the next section.

3 Antenna designs and simulated performances

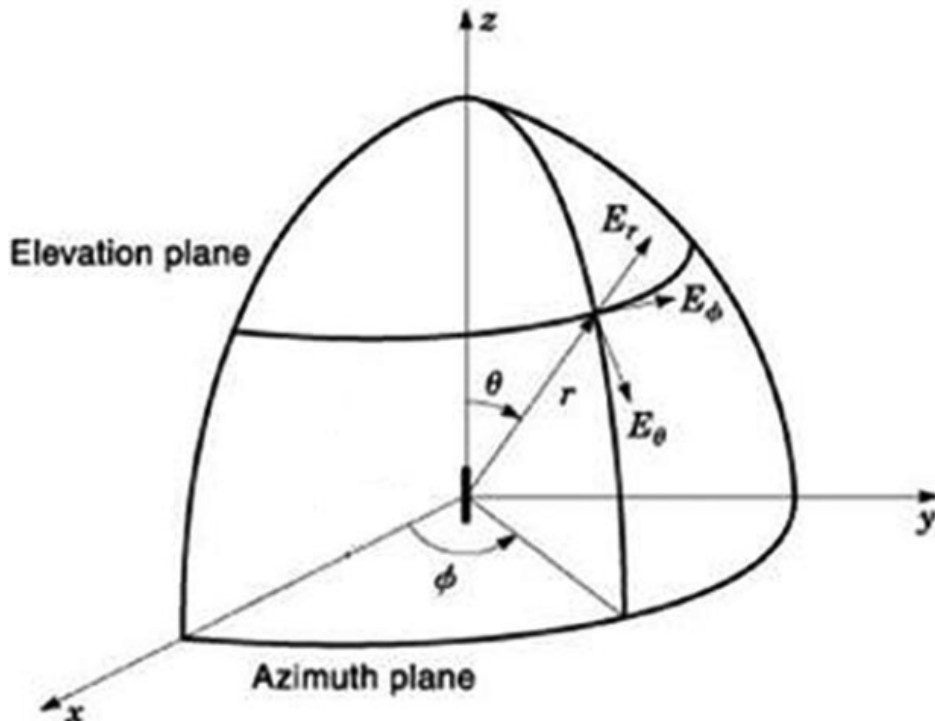
In this section, the different antenna designs are highlighted and their simulated radio-electrical properties are presented. A comparison between the design with a simplified and complete model illustrates the impact of the MB1623 board.

3.1 Used coordinates for gain patterns

For each antenna topology, the coordinates shown in Figure 2 are used. The gain patterns are assessed in three planes of interest:

- XoZ: $\Phi = 0^\circ$, $\theta = -180$ to $+180^\circ$.
- YoZ: $\Phi = 90^\circ$, $\theta = -180$ to $+180^\circ$.
- XoY: $\theta = 90^\circ$, $\Phi = -180$ to $+180^\circ$.

Figure 2. Coordinate system used in simulations for the gain patterns



3.2 Monopole T-shaped antenna

3.2.1 Configuration

Many investigations are conducted in the literature to propose monopole [1] antennas based on different shapes, such as the meander [1] proposed in 1991, and having the property to be scannable to any angle between -90° and 90°. Another different work is presented in [2], where several experiments are carried out on various planar monopole antennas such as elliptical, rectangular, circular, hexagonal disc and square monopoles. The maximum bandwidth is achieved for elliptical disc shape.

Regarding the requirements and specifications, a simple design allowing a single band operation is chosen.

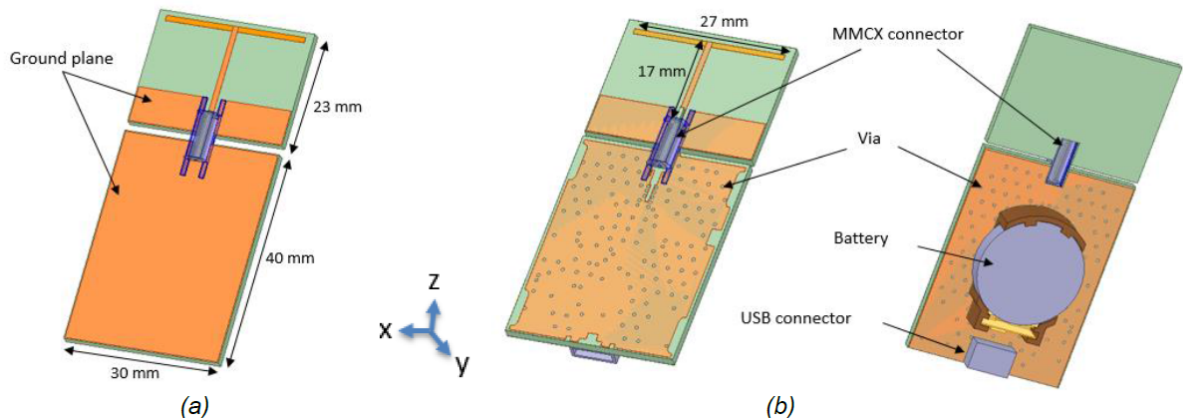
Figure 3 shows the structure of the T-shaped planar monopole antenna excited by a coplanar waveguide line. The MMCX connector aims to link the antenna PCB to the MB1623 board. The antenna dimensions are optimized to achieve impedance matching at the desired frequency in the ISM band around 2.45 GHz.

The first simulation is performed based on a simple design as shown in Figure 3 (a). A simple PCB is designed by using Grounded FR4 substrate, and associated with the T-antenna using a $50\ \Omega$ MMCX connector.

To approximate the structure's real model, a complete design as illustrated in Figure 3 (b) is constructed. It contains all the critical elements that can influence the antenna performances such as the battery, the USB connector and the vias allowing connection between the ground planes.

The overall size of the structure, antenna, and MB1623 board, is $30 \times 63\text{ mm}^2$ and the substrate used here has the following characteristics: a dielectric constant of = 4.4, a loss tangent of = 0.02, and a thickness of $h = 1.6\text{ mm}$.

Figure 3. Monopole T-shaped antenna configuration: (a) simplified model (b) complete model



3.2.2 Simulation results

The simulated reflection coefficient of the two previously presented models in Figure 3 is shown in Figure 4. It can be observed that a wide bandwidth is obtained, ranging from 1.52 to 2.63 GHz with a good impedance matching all over the bandwidth of interest which is, in this case, the ISM band. A negligible difference is noticed between the simple and complete model in terms of the reflection coefficient that falls from -24 to -18 dB at 2.4 GHz. However, this fall remains acceptable and it is particularly due to losses generated by the insertion of the real environment components, such as battery and connectors.

Figure 4. Simulated return loss versus frequency for simple and complete models

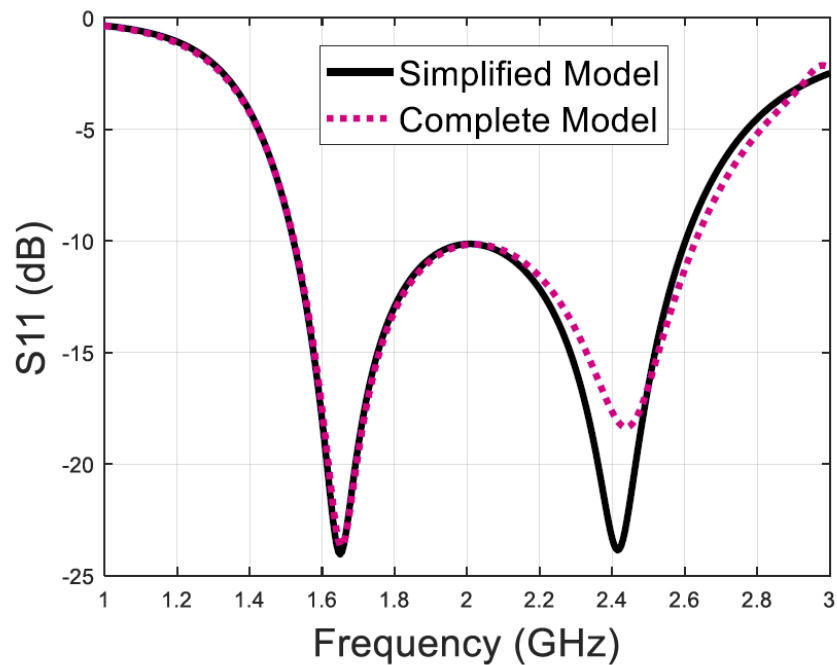


Figure 5 is mainly used here to show the response of the input impedance for the simplified and complete designs. It can be noted that the real and imaginary parts are almost identical for both designs, which confirms that there is no significant effect caused by the real antenna context. However, according to Figure 6, the total efficiency decreases by 3 % for the complete antenna model compared to the simple one, which is expected, because of material losses, such as solder mask, substrate, and cooper. A smooth resonance near 2 GHz can be observed, which explains the wide impedance matching. This resonance is linked to the presence of the MB1623 board.

Figure 5. Simulated input impedance versus frequency for simple and complete models

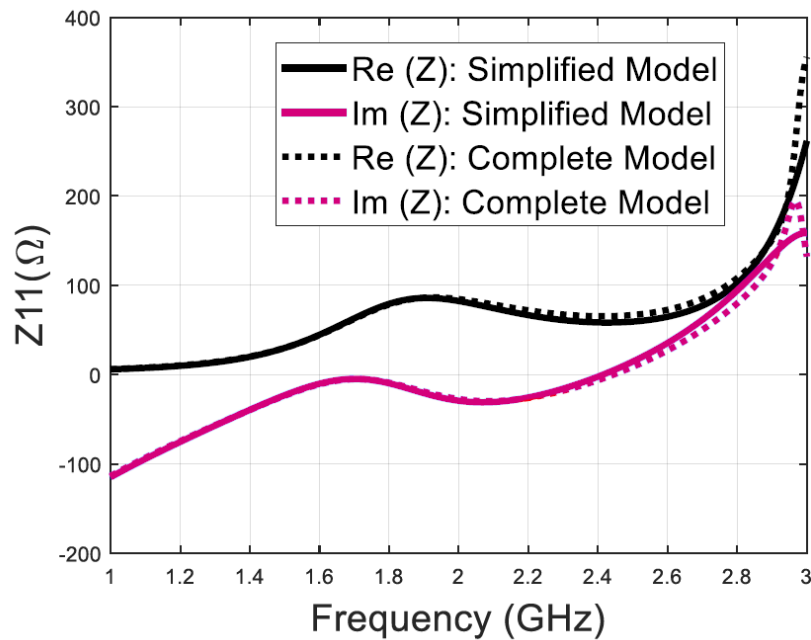


Figure 6. Simulated total efficiency versus frequency for simple and complete models

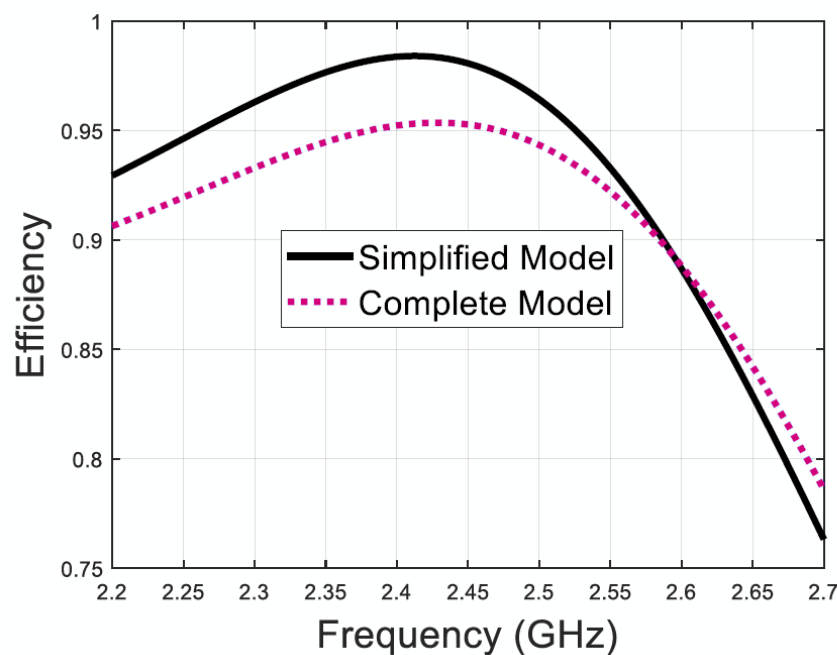
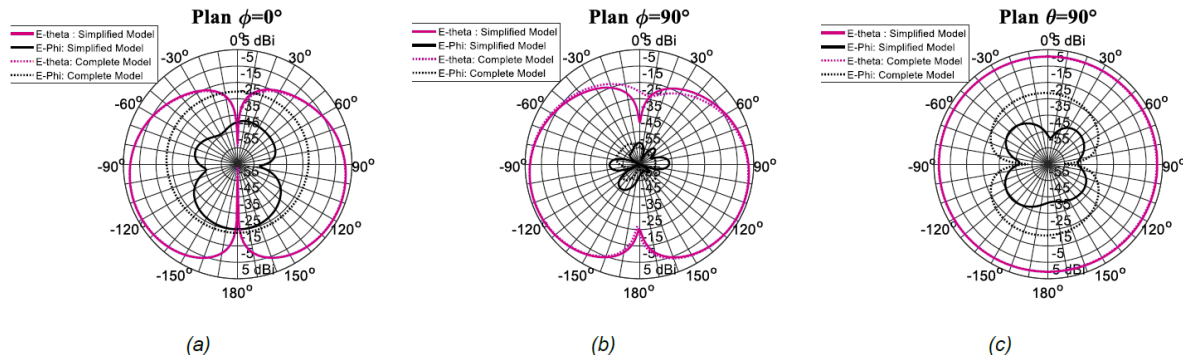


Figure 7 illustrates the radiation pattern performances for the T-shaped antenna following the three planes: $\phi=0^\circ$, $\phi=90^\circ$, and $\Theta=90^\circ$. There is an omnidirectional behavior in the $\Theta=90^\circ$ plane. Moreover, the simulation results of the simplified model agree very well with the complete one. However, the cross-polarization level increases in the case of the complete design, which is essentially due to the battery insertion in the PCB.

Figure 7. Simulated radiation pattern for the simplified and complete models at 2.45 GHz: (a) $\phi=0^\circ$: XZ plane, (b) $\phi=90^\circ$: YZ plane, (c) $\Theta=90^\circ$: XY plane



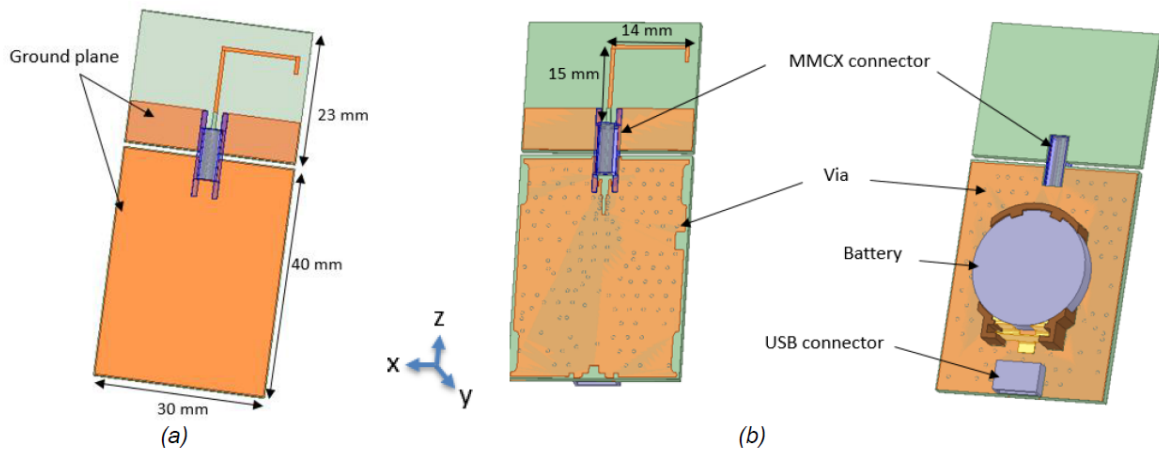
3.3 Monopole L-shaped antenna

3.3.1 Configuration

The antenna under study here is the basic L-shaped monopole antenna. The design consists of three radiating arms. Regarding the dimensions requirements, the antenna shape is optimized to adjust the resonance frequency, by adding a small extension. The length of the radiating elements is tuned to achieve good impedance matching at the desired operating frequency of 2.45 GHz. The overall antenna dimensions, including the PCB board, are 30 x 63 mm².

The substrate used is FR4 with the same characteristics as mentioned in the previous design. The simplified and the complete model, as presented in Figure 8, are studied and compared here.

Figure 8. Monopole L-shaped antenna configuration: (a) simplified model (b) complete model



3.3.2 Simulation results

Figure 9 depicts the simulation results of the reflection coefficient versus frequency variation. As observed, the antenna radiates over a wide range of frequencies, with good impedance matching around 2.45 GHz.

A small degradation of the return loss of -7 dB is perceived in the case of the complete model compared to the simplified one, but this does not affect the antenna performances.

Concerning the input impedance, the variation of the real and imaginary parts within the frequency, are represented in Figure 10. A good agreement is detected for the complete and simplified model, which proves that the real environment has no effect on the antenna input impedance. Once again, the smooth resonance due to the chipboard is observable and helps to wideband input impedance matching.

Figure 9. Simulated return loss versus frequency for simple and complete models

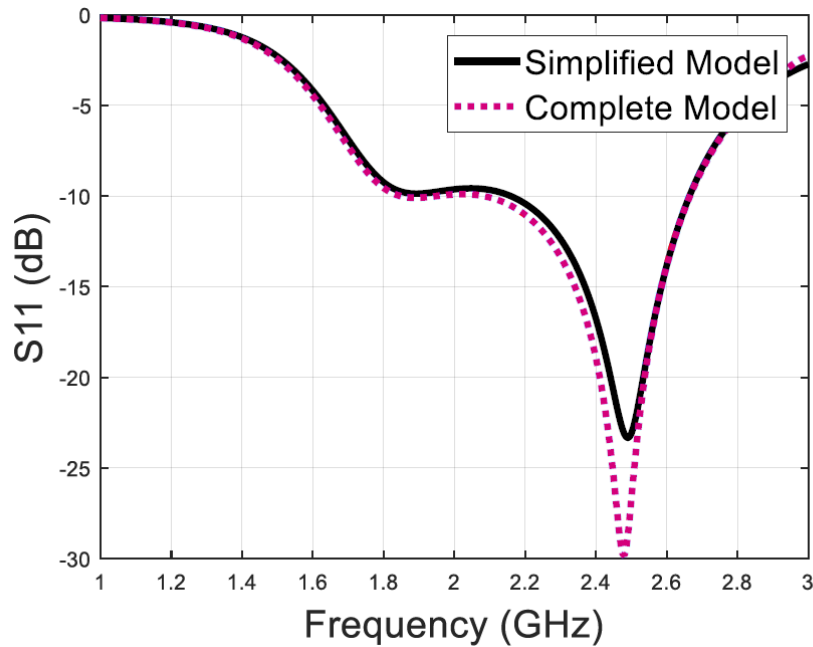


Figure 10. Simulated Input impedance versus frequency for simple and complete models

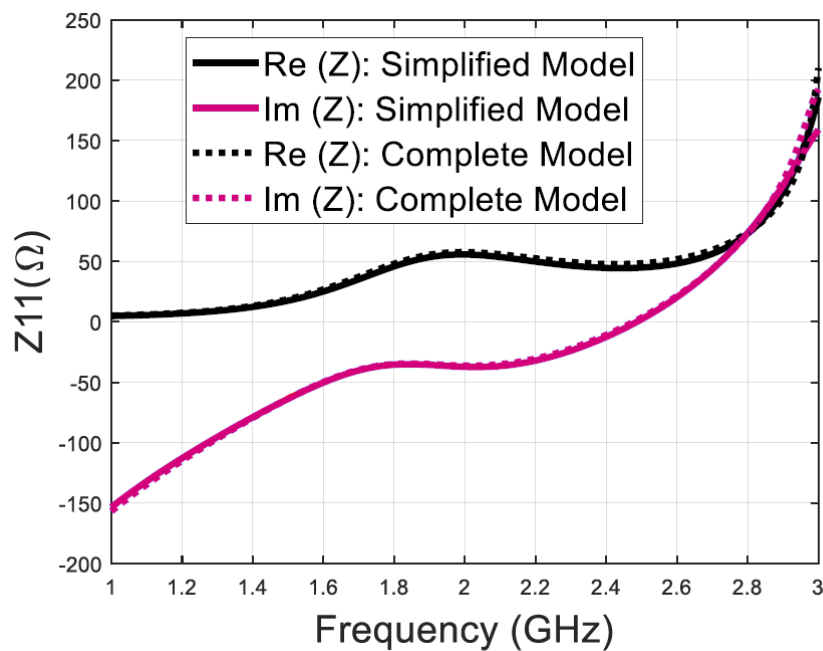


Figure 11 describes the total efficiency variation within the frequency. The complete antenna model shows 1.7 % degradation in terms of total efficiency, like the previous design, but the values remain acceptable.

The radiation patterns are exposed in Figure 12 in the three planes. The 3D representation shows a quasi-broadside behavior within the $\phi=0^\circ$ plane. Furthermore, the cross-polarization level increases with the complete antenna model.

Figure 11. Simulated efficiency versus frequency for simple and complete models

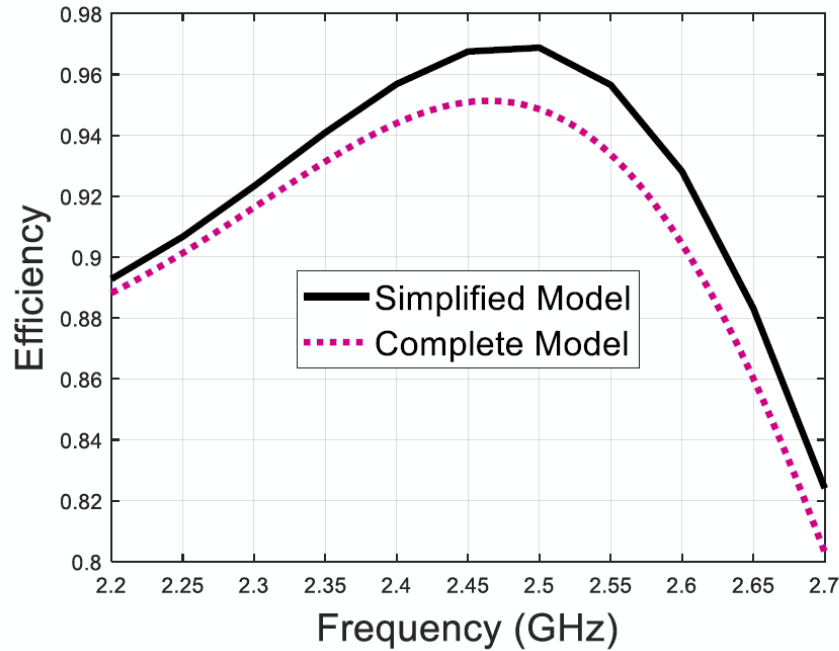
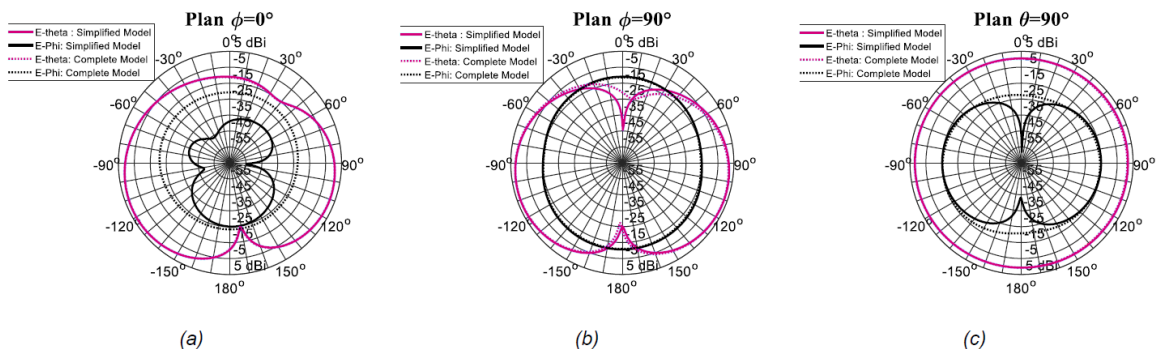


Figure 12. Simulated radiation pattern for the simplified and complete models at 2.45 GHz: (a) $\phi=0^\circ$ (XZ plane), (b) $\phi=90^\circ$: (YZ plane), (c) $\Theta=90^\circ$: (XY plane)



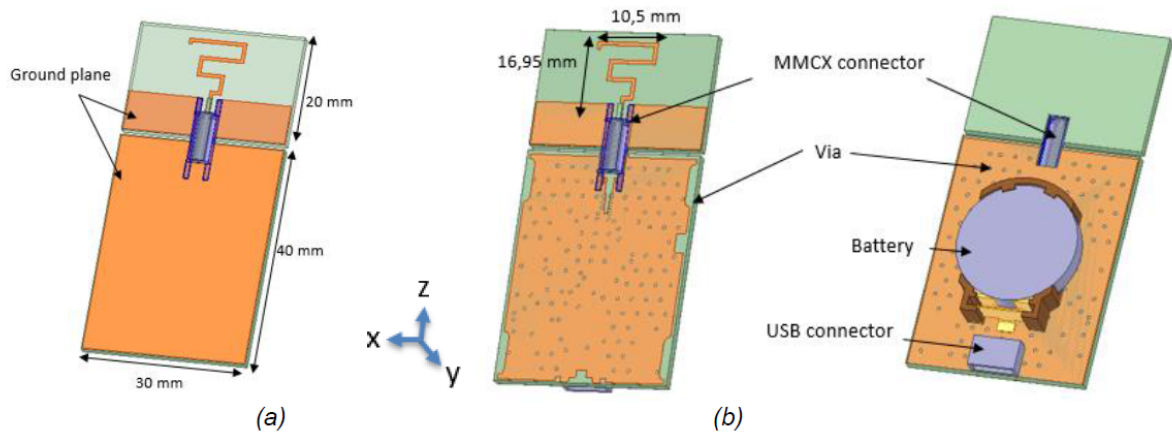
3.4 Meander line antenna

3.4.1 Configuration

The proposed radiating element consists of a meander line antenna presented in [5], based on its a V-shaped, for which the meander line length, as well as the shape, is optimized to accomplish good impedance adaptation around the operating frequency of 2.45 GHz.

For this design also, the same context is used in the simulation. The structure's size is $50 \times 30 \text{ mm}^2$, as presented in Figure 13.

Figure 13. Meander line antenna configuration: (a) simplified model (b) complete model



3.4.2 Simulation results

The simulated reflection coefficient across the frequency range from 1 to 3 GHz is shown in [Figure 14](#). The structure resonates at 2.45 GHz with an S11 better than -10 dB within the ISM band. The operating bandwidth is maintained despite the transition to the complex model. Otherwise, as exposed in [Figure 15](#), the input impedance results demonstrate good stability in terms of real and imaginary parts whatever the studied model. Once again, the smooth resonance due to chip PCB is observed and it helps to widen the operating band.

Figure 14. Simulated reflection coefficient versus frequency for simple and complete models

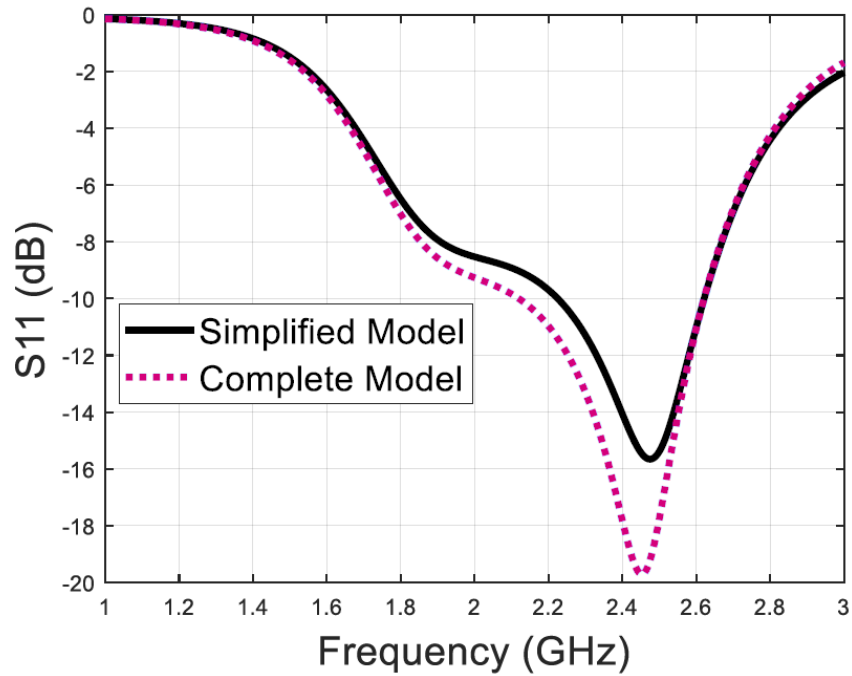
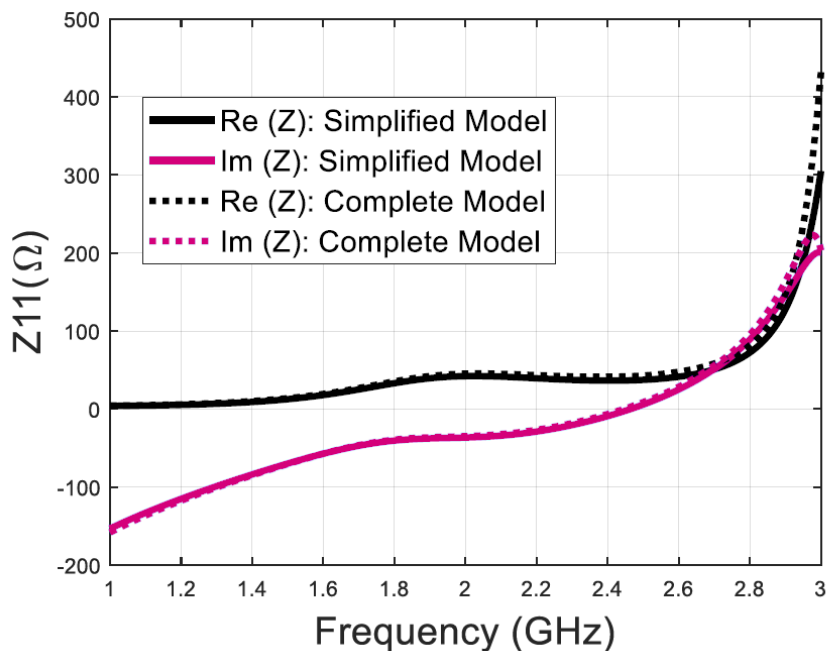


Figure 15. Simulated input impedance versus frequency for simple and complete models

The total efficiency of the antenna near the resonance frequency in the range from 2.2 to 2.7 GHz is also verified as plotted in [Figure 16](#). A maximum of 92 % is obtained with the complete model, with a slight decrease of approximately 1 % compared to the basic model. The antenna radiation patterns for φ and Θ polarized components are illustrated in [Figure 17](#). The radiation power pattern shows an omnidirectional behavior following the $\Theta=90^\circ$ plane.

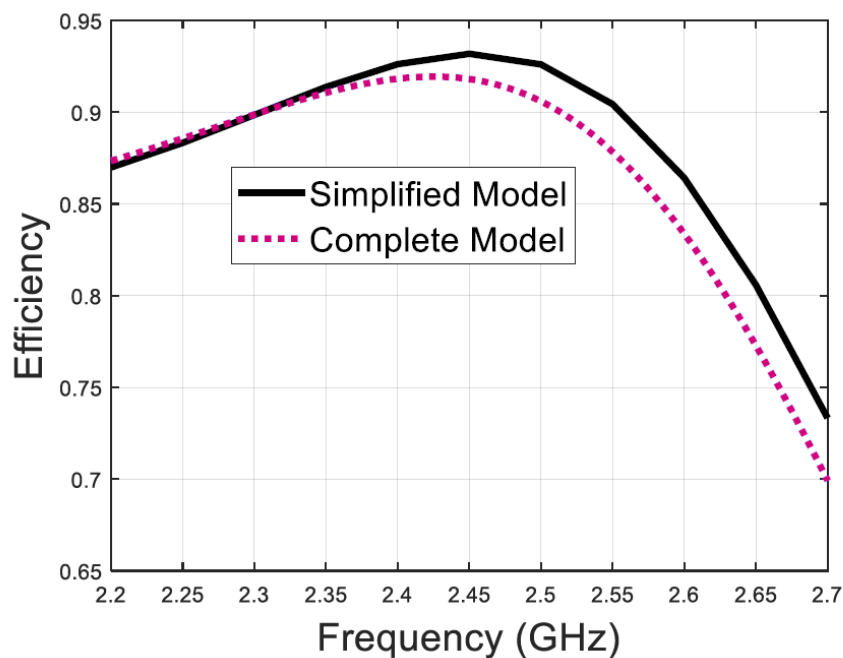
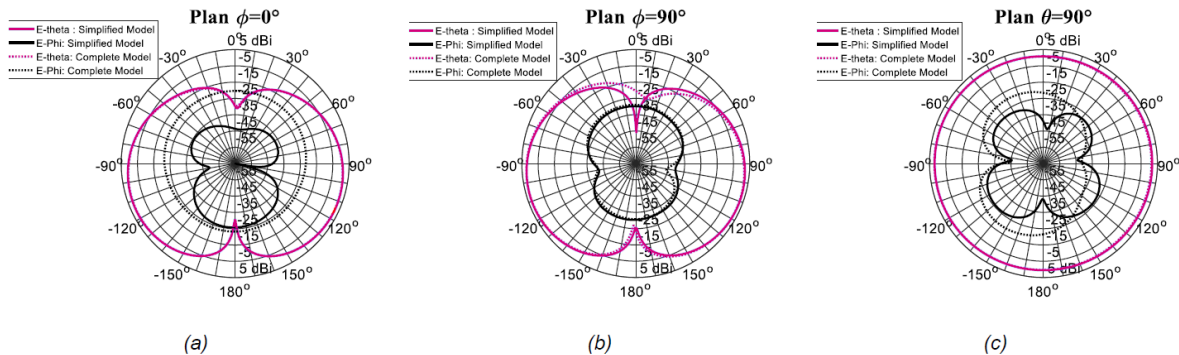
Figure 16. Simulated efficiency versus frequency for simple and complete models

Figure 17. Simulated radiation pattern for the simplified and complete models at 2.45 GHz: (a) $\varphi=0^\circ$ (XZ plane), (b) $\varphi=90^\circ$ (YZ plane), (c) $\Theta=90^\circ$ (XY plane)



3.5 Inverted F antenna - IFA

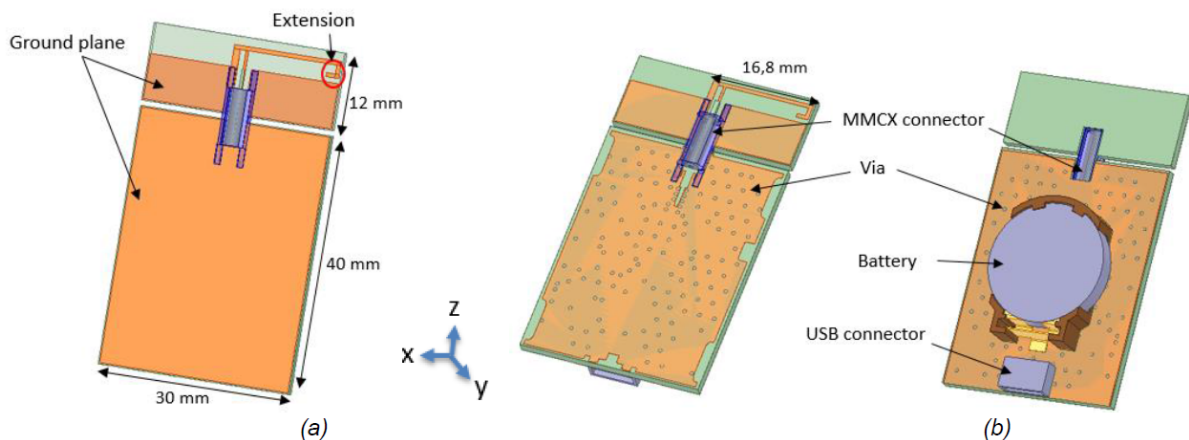
3.5.1 Configuration

Numerous research studies are conducted to analyze the Inverted-F antenna such as in [4] where the authors present experimental observations about the IFA performances at the frequency 1.8 GHz for portable handsets.

The 3D inverted-F antenna is also explored in the presence of parasitic elements in 1989 by H.Nakano and his colleagues[5], to reveal the behavior of the input impedance and to widen the impedance bandwidth.

Similarly, the geometry and dimensions of the proposed inverted F antenna conceived here, are shown in Figure 18. The simplified and complete designs are also investigated here to ensure good accuracy results. This design is compact compared to the previous ones with an overall size of $52 \times 30 \text{ mm}^2$. Additionally, to optimize the location of the radiating element on the small PCB, an L-shaped extension is added to achieve resonance at the desired frequency without increasing the PCB dimensions as presented in Figure 18 (a).

Figure 18. Inverted-F antenna configuration: (a) simplified model (b) complete model



3.5.2 Simulation results

The proposed IFA models are designed also on the FR4 substrate based on dimensions shown in Figure 18. The simulated return loss for the simplified model is shown as a black line, while the complete one is as a dashed red line in Figure 19. A slight shift of the resonance frequency can be observed when the antenna is placed on its real environment. However, a good reflection coefficient is maintained over the ISM range of frequencies. Notice that the resonance associated with the chip PCB is not excited with this compact antenna topology and the matching frequency band is consequently narrower.

In Figure 20, the simulated input impedance variation within frequency is exposed. An insignificant difference is observed in terms of real and imaginary parts when switching to a complete model.

Figure 19. Simulated return loss versus frequency for simple and complete models

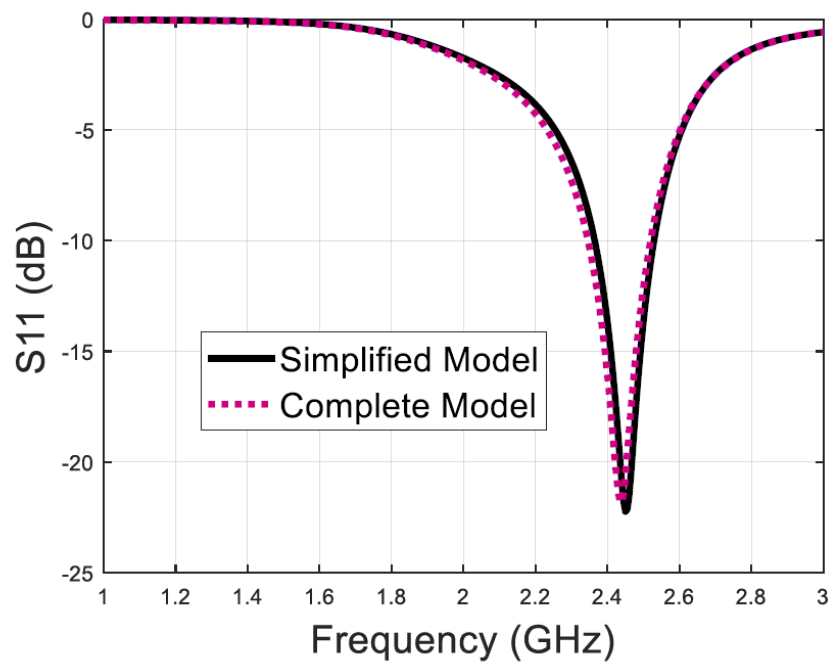


Figure 20. Simulated input impedance versus frequency for simple and complete models

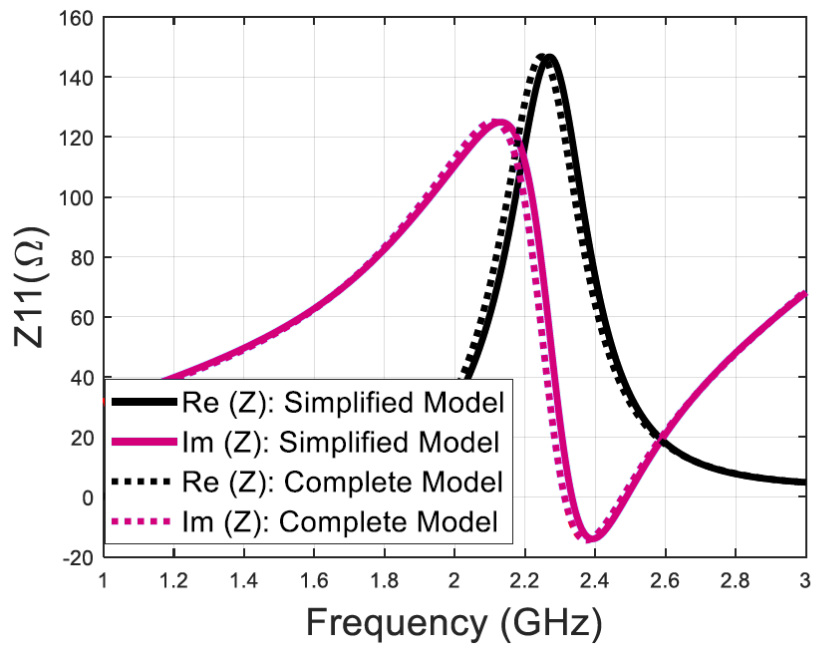


Figure 21 illustrates the total efficiency of the IFA antenna against frequency. A decrease of 1.6 % is observed in the case of the complete model compared to the simple one. Figure 22 shows the 2D radiation pattern in terms of gain, in three different planes at 2.45 GHz. Omnidirectional radiation is observed in the plane $\Theta=90^\circ$. Notice that a good agreement is achieved between the complete and simplified models, except the cross-polarization level that increases in the $\phi=0^\circ$ and $\Theta=90^\circ$. The asymmetry of the diagram is observable in the $\phi=0^\circ$ cut plane due to antenna topology.

Figure 21. Simulated efficiency versus frequency for simple and complete models

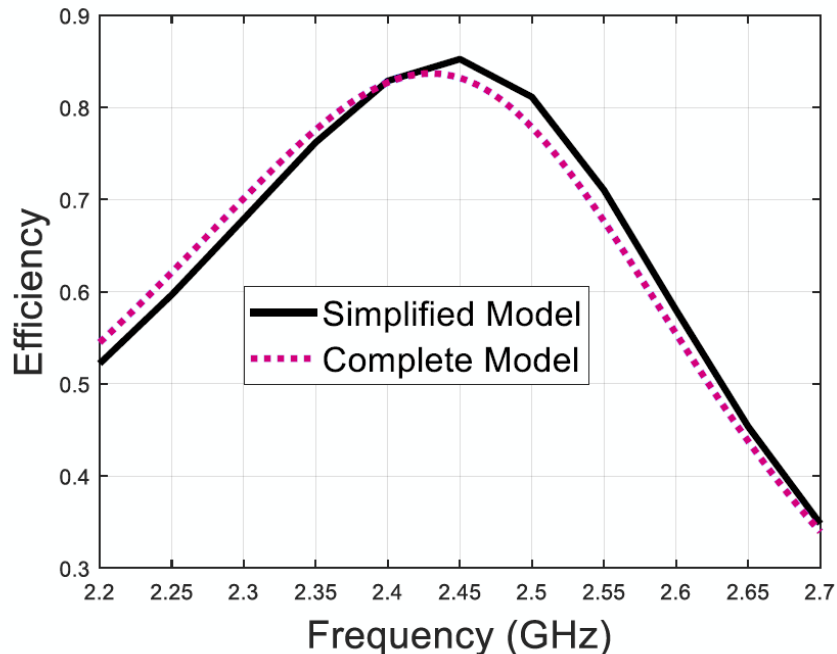
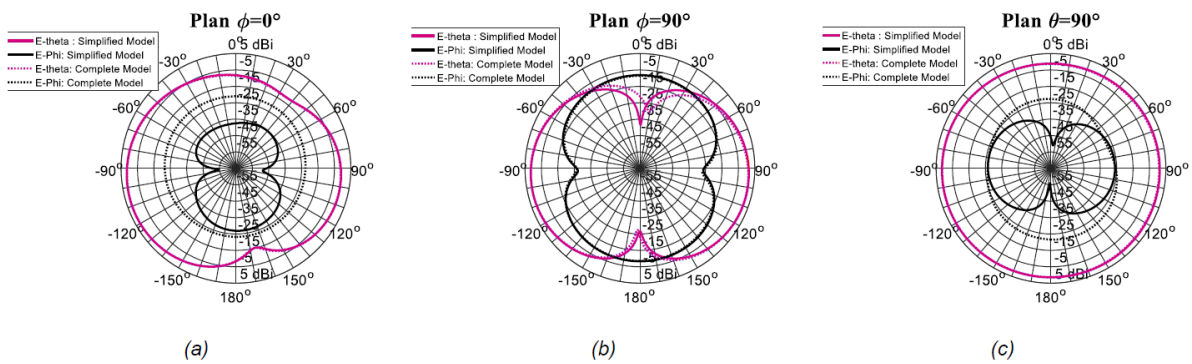


Figure 22. Simulated radiation pattern for the simplified and complete models at 2.45 GHz: (a) $\phi=0^\circ$ (XZ plane), (b) $\phi=90^\circ$ (YZ plane), (c) $\Theta=90^\circ$ (XY plane)



3.6

Metallic inverted F antenna

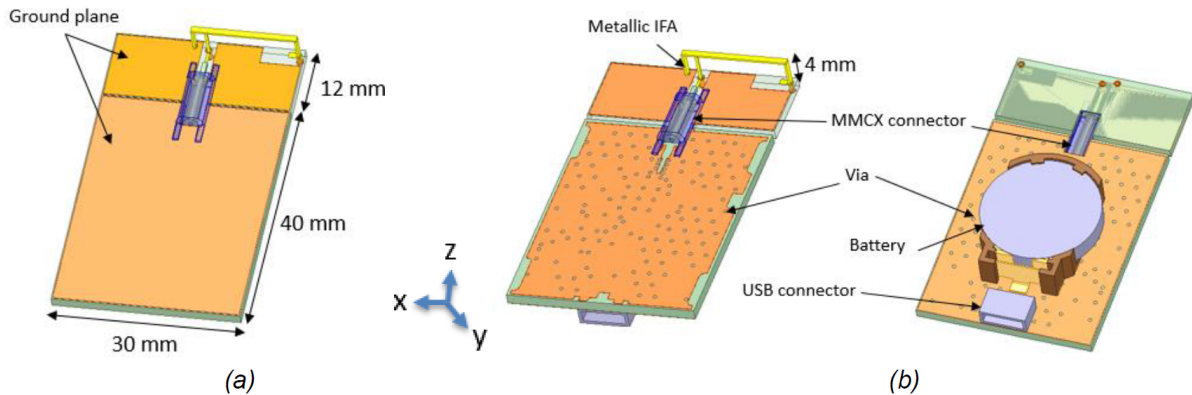
3.6.1

Configuration

The geometrical configuration of a simple Metallic Inverted F Antenna is studied as shown in Figure 23. It is soldered on the FR-4 substrate and consists of a bent monopole parallel to the PCB with a short circuit implemented arm. Basic and complete models are investigated and compared in terms of radio-electrical performances.

Regarding the constraints in terms of dimensions limitation, as well as the radiating element location that affects the impedance matching, the antenna is expanded by folding it at its extremity, to ensure on one hand a resonance at the ISM band, and on another hand a good size optimization and mechanical rigidity.

Figure 23. Metallic inverted F antenna configuration: (a) simplified model (b) complete model



3.6.2 Simulation results

The simulated return loss against frequency is as represented in Figure 24. The agreement between basic and complete model is good. The antenna is well matched to $50\ \Omega$ impedance and provides a return loss of -13 dB at 2.45 GHz.

Figure 25 illustrates the variation of the input impedance versus frequency. Good stability can be noticed for the real and imaginary parts except for the maximum points for which a small decrease for the complete model is observed.

Figure 24. Simulated return loss versus frequency for simple and complete models

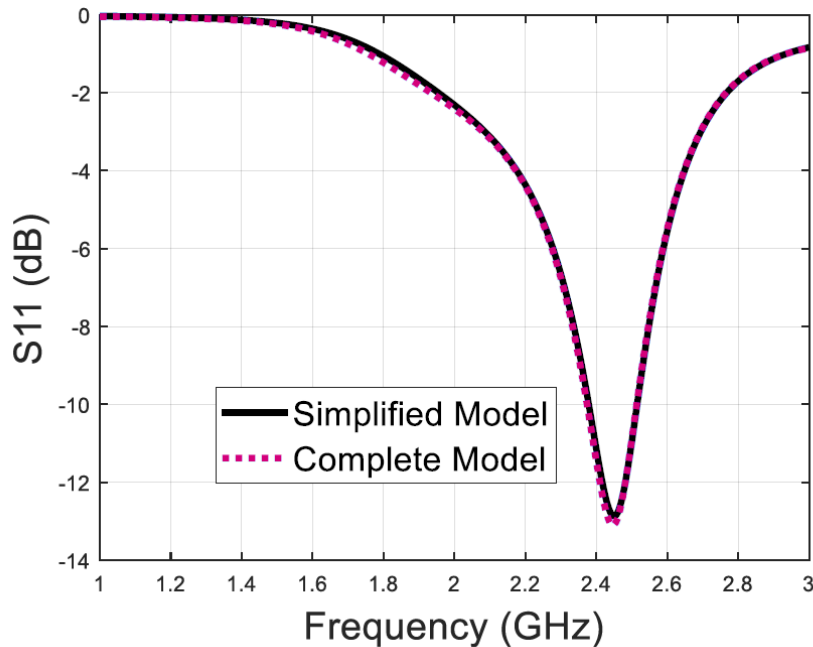


Figure 25. Simulated input impedance versus frequency for simple and complete models

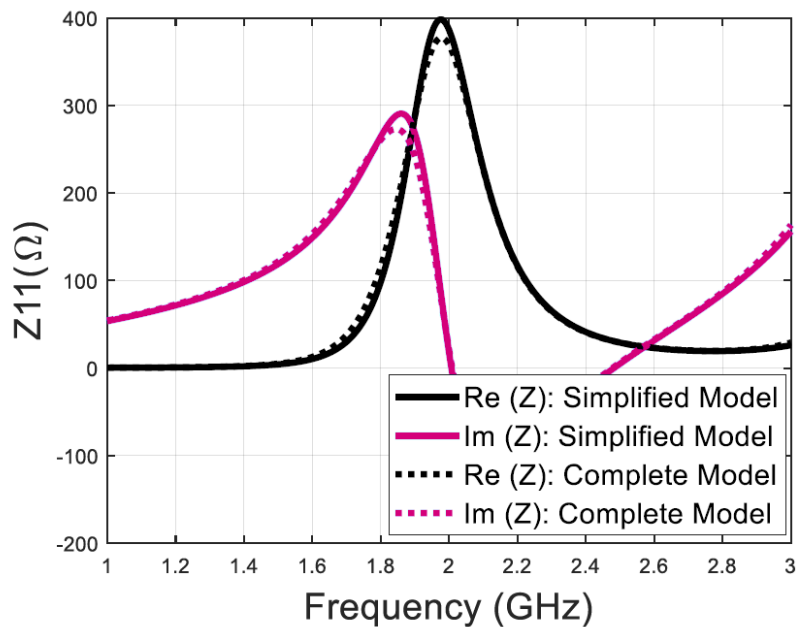


Figure 26 presents the impact of the context (complete model) on the antenna efficiency. A small peak efficiency drop of approximately 1 % is noticeable, but this remains largely acceptable.

Figure 27 exposes the variation of the 2D radiation pattern following the three principal planes at 2.45 GHz. Omnidirectional comportment is perceived following $\Theta=90^\circ$ plane, while a quasi-broadside one is observed in $\varphi=0^\circ$ plane. The radiation appears less symmetrical in the $\varphi=0^\circ$ and $\varphi=90^\circ$ cut planes compared to the printed IFA.

Figure 26. Simulated efficiency versus frequency for simple and complete models

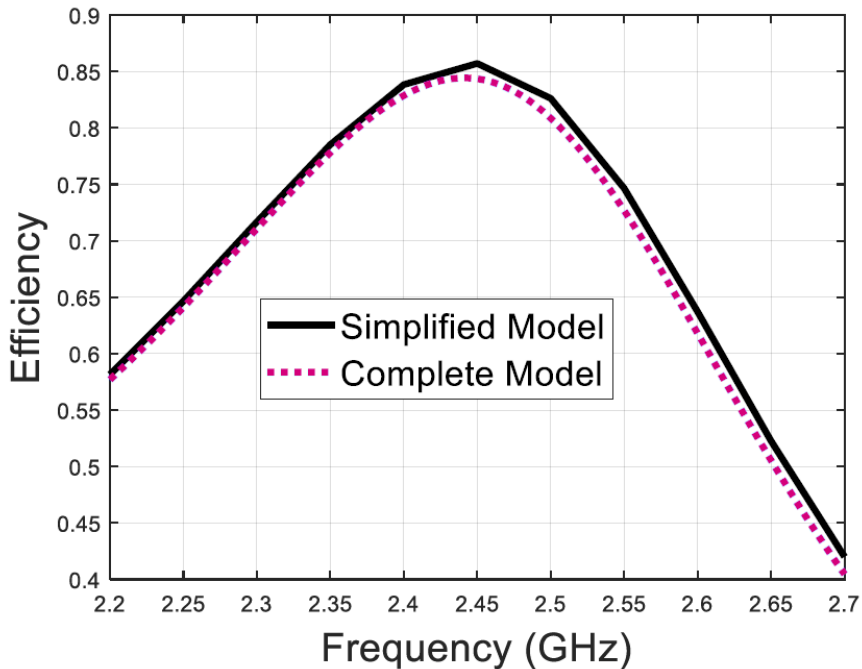
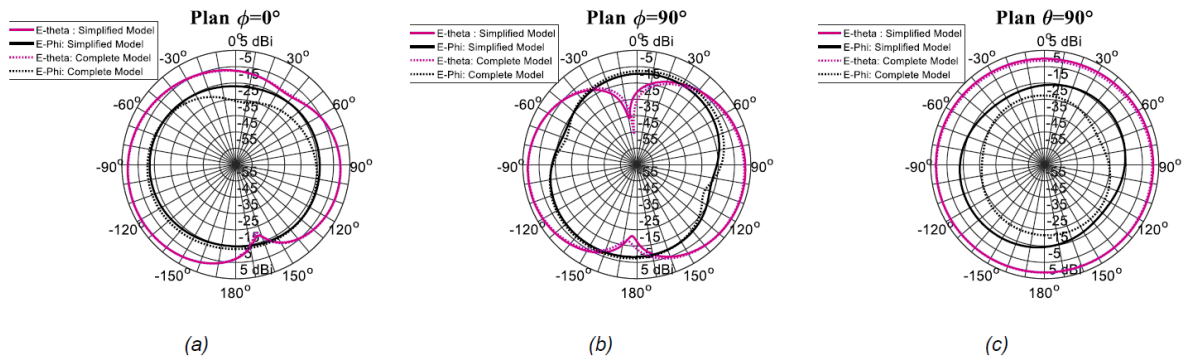


Figure 27. Simulated radiation pattern for the simplified and complete models at 2.45 GHz: (a) $\varphi=0^\circ$ (XZ plane), (b) $\varphi=90^\circ$ (YZ plane), (c) $\Theta=90^\circ$ (XY plane)



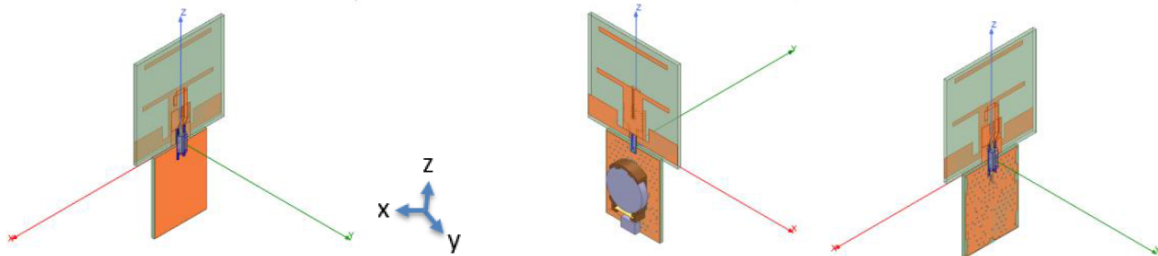
3.7 Yagi-Uda antenna

3.7.1 Configuration

Yagi-Uda antennas are used for a long time due to their end-fire radiation and relatively high gain [7]. Typically, a Yagi-Uda antenna includes an exciter with one reflector and one or more directors.

To have the antenna and MB1623 board in the same plane, a dual-layer dipole is selected. In such configuration, the feeding line is on one layer and the radiating elements are on the second layer. The optimized structure is shown in Figure 28. The feed printed dipole uses an incorporated Marchand balun to correctly excite the antenna. The size of the antenna is $50 \times 50 \text{ mm}^2$.

Figure 28. Geometry of the Yagi-Uda antenna



3.7.2 Simulation results

The simulated reflection coefficient versus frequency is presented in Figure 29. The difference between the simplified and the complete model is very small. The reflection coefficient is lower or equal to -10 dB from 2.4 to 2.48 GHz.

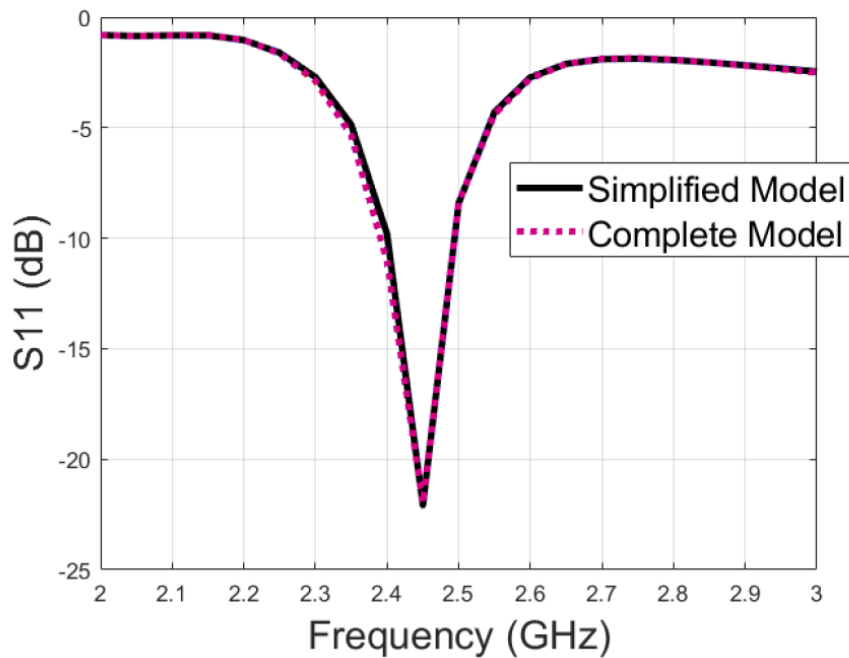
Figure 29. Simulated reflection coefficient of the Yagi-Uda antenna

Figure 30 shows the simulated complex input impedance of the optimized Yagi-Uda antenna at the MMXC connector of the antenna. The real part is close to $50\ \Omega$ in the band of interest and the imaginary part is close to 0.

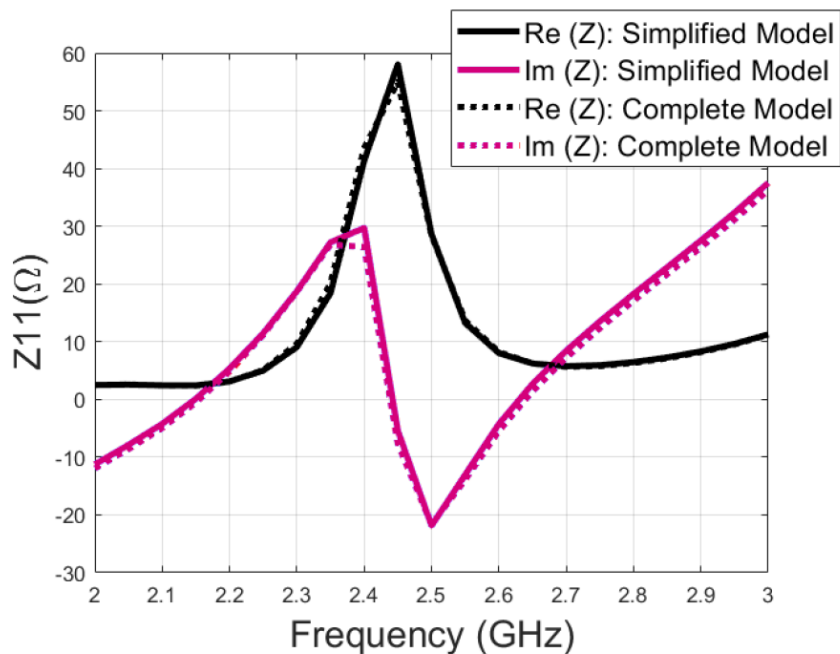
Figure 30. Simulated input impedance of the Yagi-Uda antenna

Figure 31 illustrates the simulated radiation efficiency of the Yagi-Uda antenna. It is greater than 70% in the 2.4-2.485 GHz band. A difference of 1.5% is observed between the complete and simplified models.

The simulated gain patterns of the Yagi are provided in Figure 32 at 2.45 GHz. A maximum gain of 5.8 dBi is achieved at $\theta=0^\circ$ and $\phi=0^\circ$. The front to back ratio is 8.1 dB. The gain patterns are almost identical for the simplified and the complete models which once again highlights the very small impact of the MB1623 board on the antenna characteristics. This is the advantage of the Yagi-Uda antenna since it presents à directional radiation oriented away from the Bluetooth® Low Energy board.

Figure 31. Simulated efficiency of the Yagi-Uda antenna

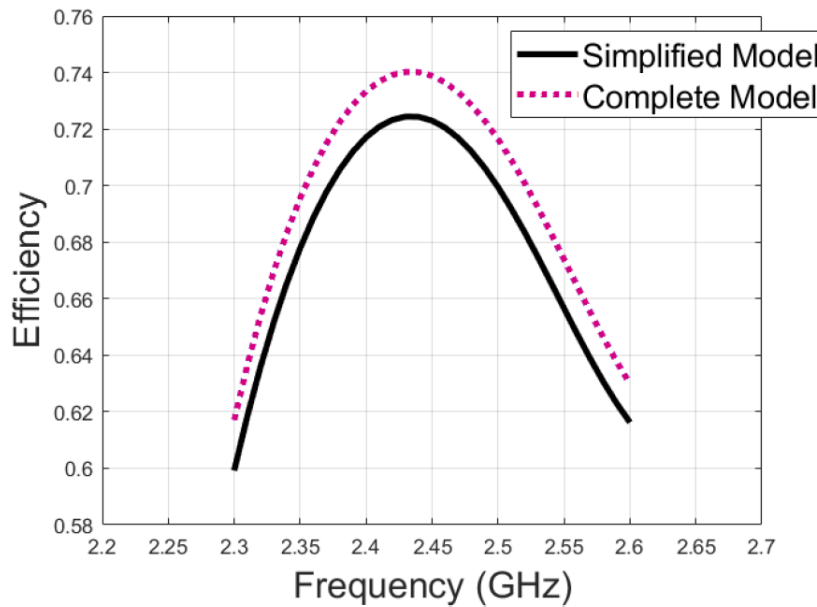
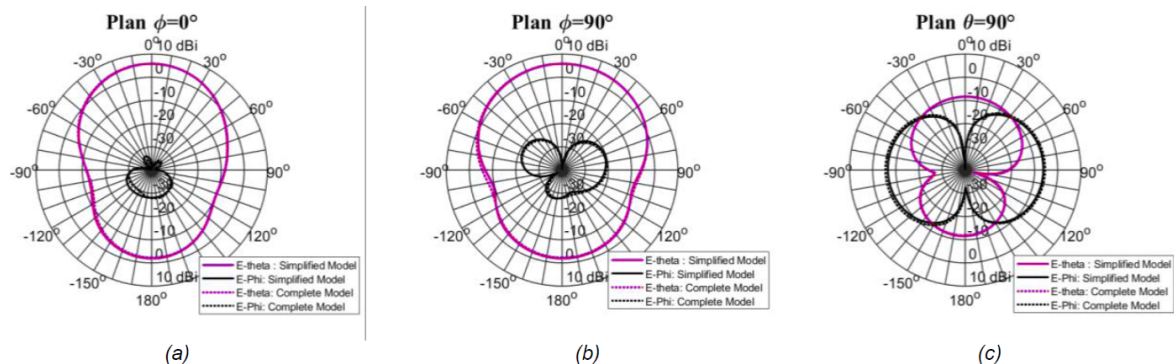


Figure 32. Simulated radiation pattern of the Yagi-Uda antenna at 2.45 GHz: (a) $\phi=0^\circ$ (XoZ plane), (b) $\phi=90^\circ$: (YoZ plane), (c) $\Theta=90^\circ$: (XoY plane)



3.8 Chip antenna

A TDK chip antenna for the 2400-2484 MHz frequency band [7] is selected as the reference antenna. It is not possible to simulate it because its electromagnetic model is not known. The layout recommended by TDK is used. The matching to $50\ \Omega$ will be carried out based on measurements with the board and antenna connected. The gain patterns are characterized once the impedance matching is performed.

4

Fabrication of the prototypes

The antenna drawings are grouped together in a single layout including breakable circuits. The properties of the layers are :

- 1.6 mm FR4 substrate
- 35 µm metallization
- 20 µm solder mask
- Metallized vias

An exploded view and pictures of the fabricated PCB are respectively shown in [Figure 33](#) and [Figure 34](#).

Figure 33. Exploded view of the layout

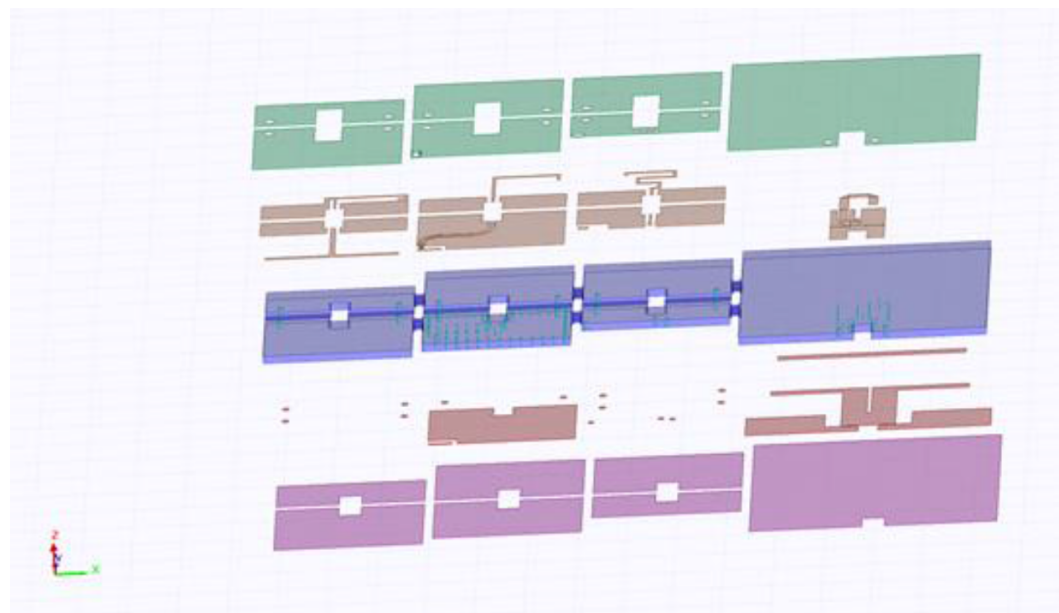
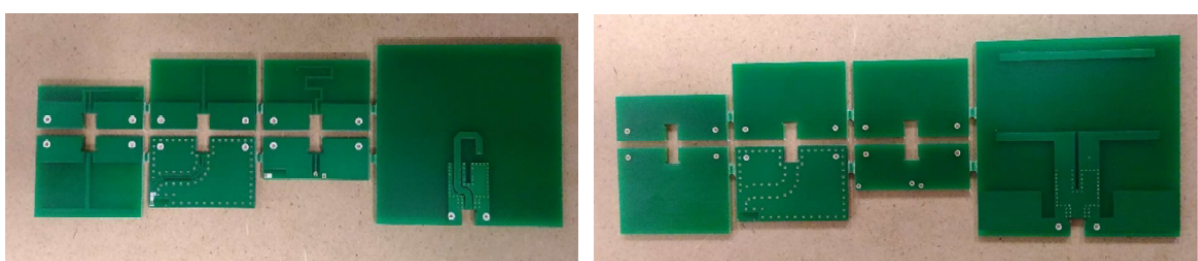


Figure 34. Pictures of the realized PCB (Top layer on the left, and bottom layer on the right)



Radio-electrical characteristics

The following section focuses on the measurement of the radio-electrical characteristics of the antenna prototypes (S11 parameter + radiation). The size of the devices is smaller than half a wavelength which requires precautions during measurements to minimize the interaction of the testing environment with the device under test (DUT). In particular, for S11 parameter measurement, the coaxial cable must be correctly soldered and positioned onto the device. Equally, for radiation measurement, a dielectric mast must be used and an optical link replaces coaxial cables to connect the DUT to the measurement instrument (Vector Network Analyser).

5 Measurement setups

This section provides some details on the measurement setups and methods used to evaluate the radiation characteristics of the different devices. All measurements are carried out inside the UHF full anechoic chamber (From 0.8 to 18 GHz).

5.1 Reflection coefficient

The reflection coefficient, also called S11, of the devices, is measured using a VNA (Vector Network Analyser R&S ZVA40) with the antennas placed inside the anechoic chamber. A conventional OSM (Open-Short-Match) calibration is performed at the end of the coaxial test cable and an offset is used to configure the reference plane to the antenna connexion. The reference plane is used to evaluate the antenna input impedance in the right position.

5.2 Gain patterns

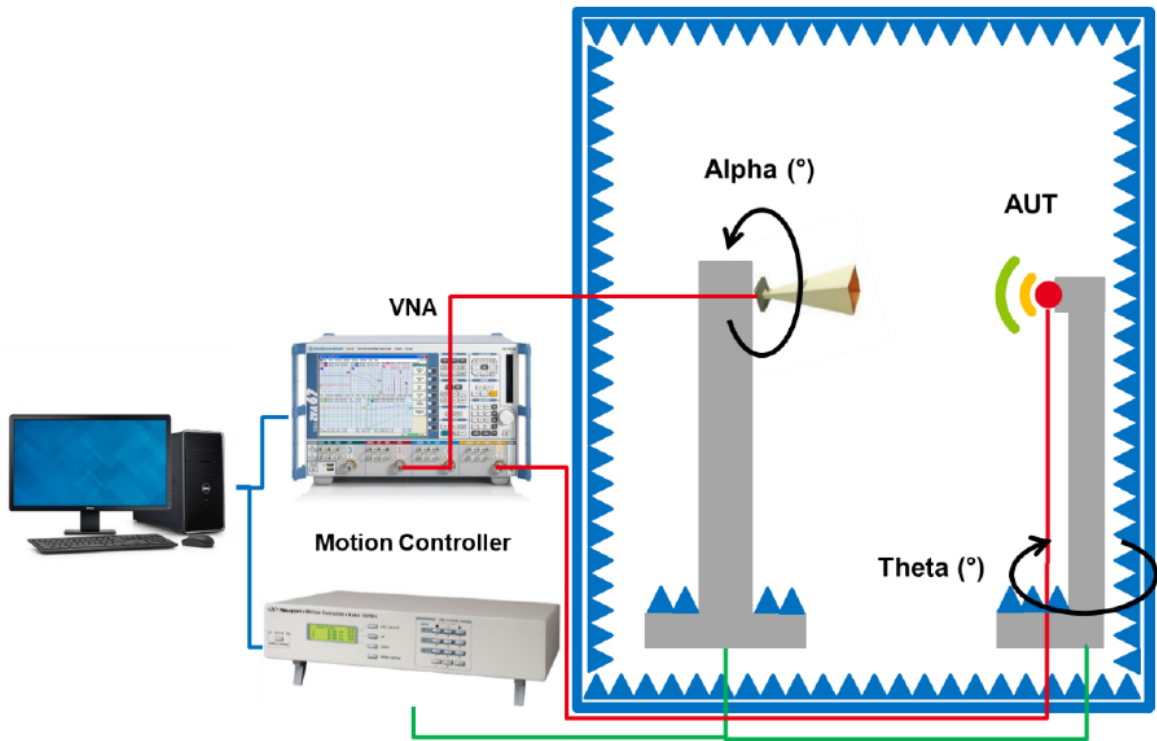
The UHF anechoic chamber is equipped with a VNA and two positioners as shown in [Figure 35](#). The analyzer and positioners are automated using software developed internally. This allows measuring gain patterns in amplitude and phase of the antenna under test (AUT) in azimuth (called a cut) using the Theta positioner at different polarization orientations using the Alpha positioner (typically 0 and 90°). Additional cut planes can be obtained by repositioning the AUT.

Given the size of the devices to be tested, the support used to mount the AUT must be minimal. The reactive distance is equal to $\lambda/(2\pi)$ which is about 2 cm at 2.45 GHz. A small polymer mast and polystyrene are used to minimize the interaction with the antenna.

An optical link replaces the traditional coaxial cable to connect the AUT to the analyzer. This is to prevent the leakage of currents from the devices to the cable grounding.

For gain measurement, the comparative method is used. In this case, a calibration is performed using a reference antenna (ETS-Lindgren's EMCO 3115) whose gain is well known. Afterward, the reference antenna is replaced by the AUT. The gain of the AUT is derived from the calibration and the gain of the reference antenna.

Figure 35. UHF anechoic chamber configuration for passive antenna measurements



5.3 Efficiency

Due to the shape of radiation, two cuts are sufficient to have a good estimation of the efficiency of an antenna by interpolating over 180 degrees and then integrating the gain pattern over the whole space. This leads to the total efficiency η by computing the integral of the far-field gain patterns.

5.4 Coordinates for gain patterns

For each antenna topology, the coordinates of Figure 35 (Refer to Section 5.2 Gain patterns) are used. The gain patterns are assessed in two planes of interest.

5.5 Measurement parameters

Table 1. Measurement parameters

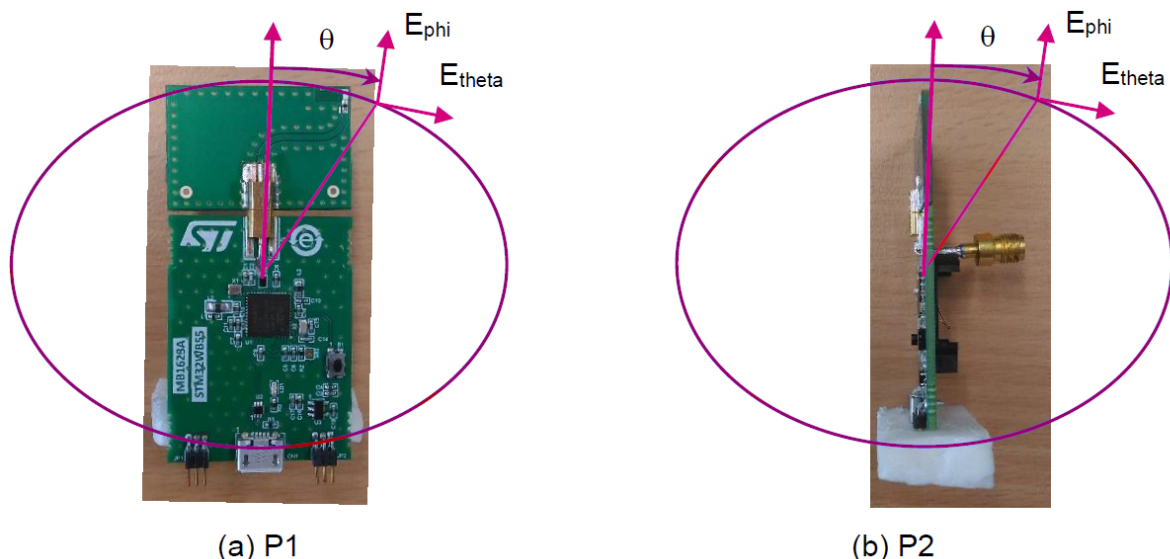
Parameter	Value
Frequency range	2.2 to 2.7 GHz
Frequency step	1 MHz
VNA IFBW	1 kHz
Averaging	5
Angular range	-180° to 180°
Angular step	2.5°

6 Measurement results

In this section, the radio-electrical properties of the 7 antenna designs are presented and overlaid to the simulation results. The antennas are measured in the following configurations as shown in Figure 36:

- P1: cut XoZ
- P2: cut YoZ

Figure 36. Antenna positioning during measurements



6.1 Monopole antennas

6.1.1 T-shaped antenna

The simulated and measured gain patterns of the T-shaped antenna associated with the MB1623 Bluetooth® Low Energy board (Figure 37) are given in Figure 38. Overall, the results are coherent. However, the short cable connected to the Bluetooth® Low Energy board for the measurements has two effects: it increases significantly the E_{phi} component in the P1 cut and it rotates slightly the E_{theta} component in the P2 cut. The maximum measured gain is 2.0 dBi at 2.45 GHz.

Figure 39 (a) displays the simulated and measured reflection coefficients. The measurements are in agreement with the simulation. The measured antenna has a reflection coefficient better than -16 dB over the Bluetooth® band (From 2.4 to 2.485 GHz). Figure 39 (b) presents the simulated and measured efficiency. The two curves are close. The minimum measured efficiency is 90 % in the Bluetooth® band.

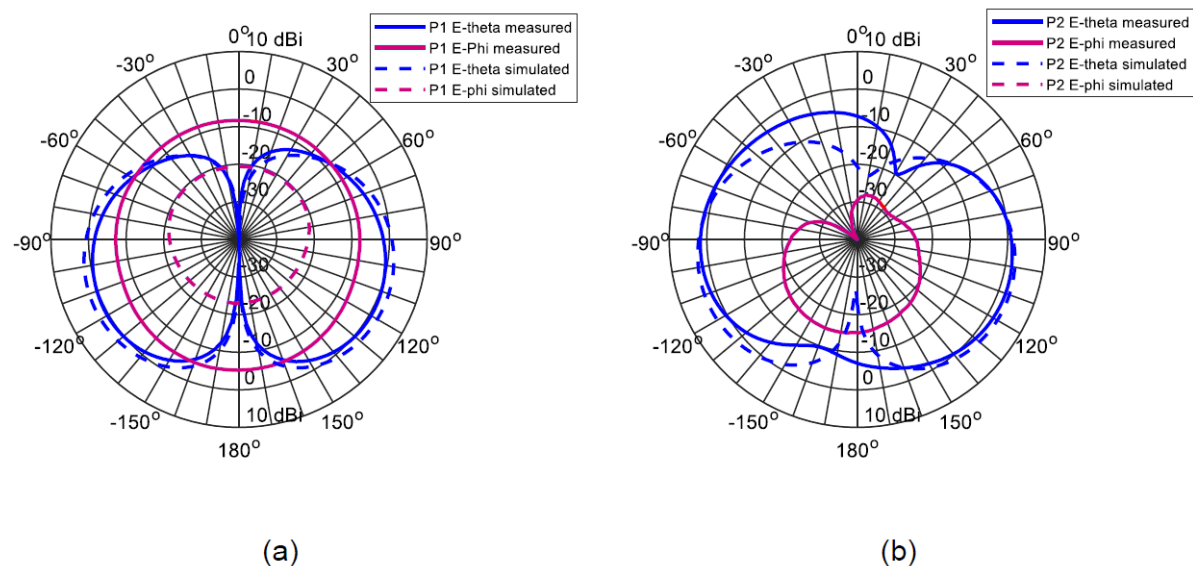
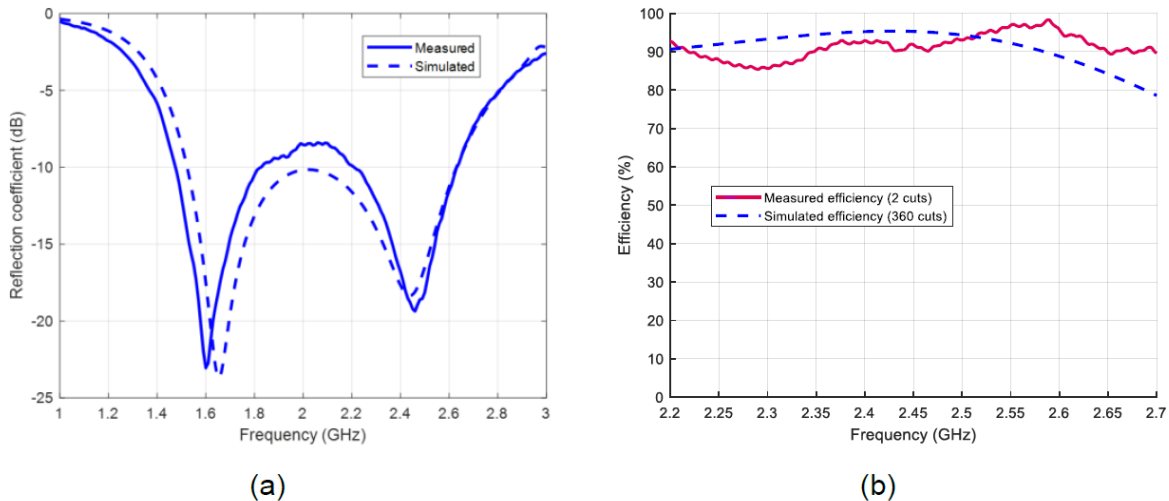
Figure 37. Monopole T-shaped antenna**Figure 38.** Gain patterns at 2.45 GHz for the P1 (a) and P2 (b) cuts

Figure 39. Reflection coefficient (a) and total efficiency (b)

6.1.2 L-shaped antenna

The simulated and measured gain patterns of the L-shaped antenna associated with the MB1623 Bluetooth® Low Energy board (Figure 40) are shown in Figure 41. Similarly to the T-shaped antenna, the short cable connected to the Bluetooth® Low Energy board increases the E_{ϕ} component in the P1 cut and rotates slightly the E_{θ} component in the P2 cut. The maximum measured gain is 1.3 dBi at 2.45 GHz.

Figure 42 (a) displays the simulated and measured reflection coefficients. The measurements are in agreement with the simulation. The measured antenna has a reflection coefficient better than -16 dB over the Bluetooth® band (From 2.4 to 2.485 GHz). Figure 42 (b) presents the simulated and measured efficiency. The two curves are close. The minimum measured efficiency is 94 % in the Bluetooth® band.

Figure 40. Monopole L-shaped antenna

Figure 41. Gain patterns at 2.45 GHz for the P1 (a) and P2 (b) cuts

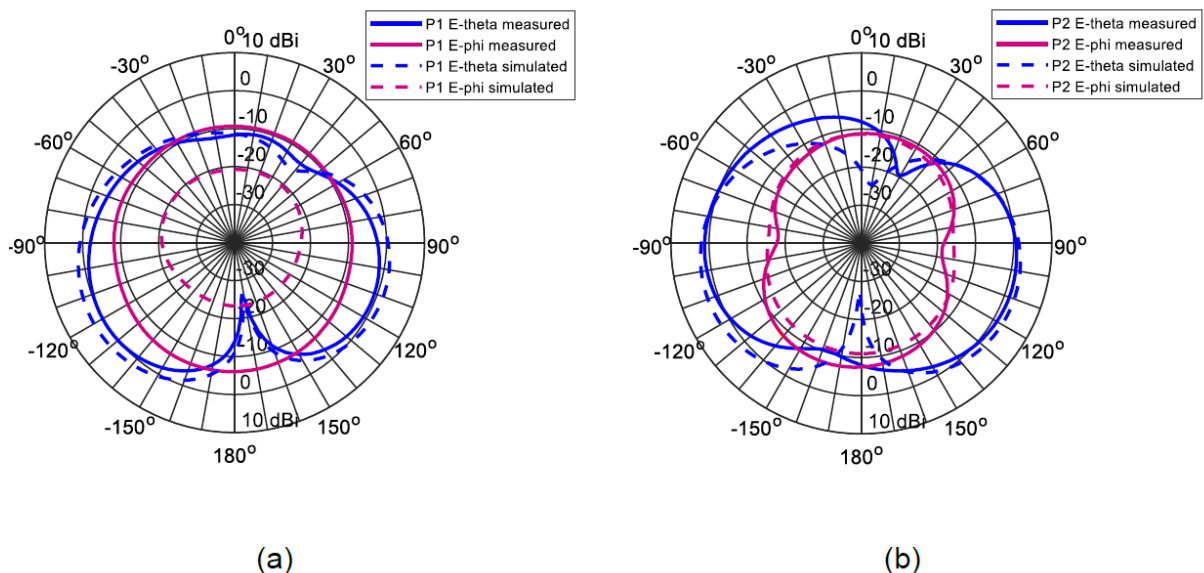
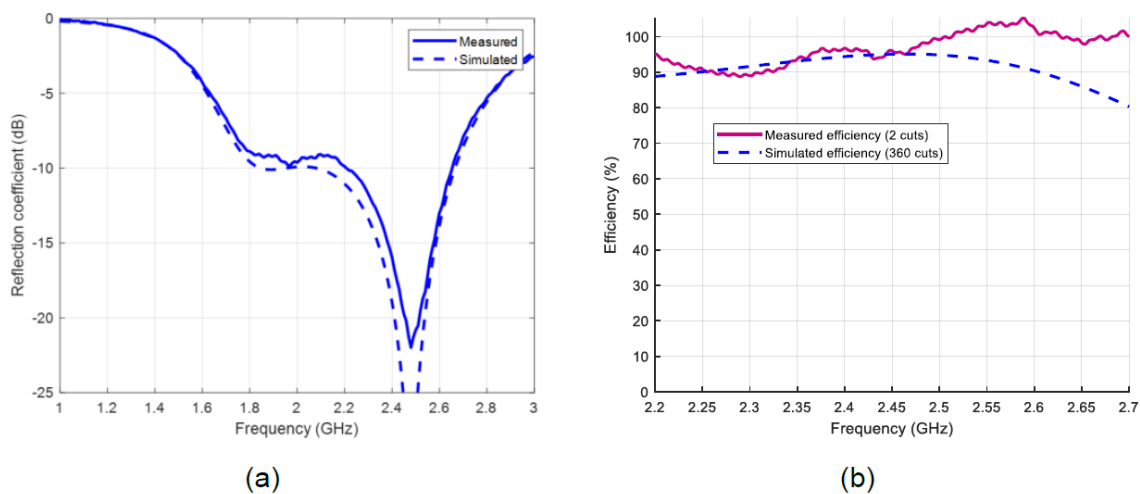


Figure 42. Reflection coefficient (a) and total efficiency (b)



6.1.3

Meander-line antenna

The simulated and measured gain patterns of the Meander-line antenna associated with the MB1623 Bluetooth® Low Energy board ([Figure 43](#)) are plotted in [Figure 44](#). Similarly to the L- and T-shaped antennas, the short cable connected to the Bluetooth® Low Energy board increases the E_{ϕ} component in the P1 cut and rotates slightly the E_{θ} component in the P2 cut. The maximum measured gain is 1.3 dBi at 2.45 GHz.

Figure 45 (a) presents the simulated and measured reflection coefficients. The measurements are in agreement with the simulation. The measured antenna has a reflection coefficient better than -18 dB over the Bluetooth® band (From 2.4 to 2.485 GHz). Figure 45 (b) presents the simulated and measured efficiency. The measurements fit the simulation. The minimum measured efficiency is 84 % in the Bluetooth® band.

Figure 43. Monopole meandered antenna



Figure 44. Gain patterns at 2.45 GHz for the P1 (a) and P2 (b) cuts

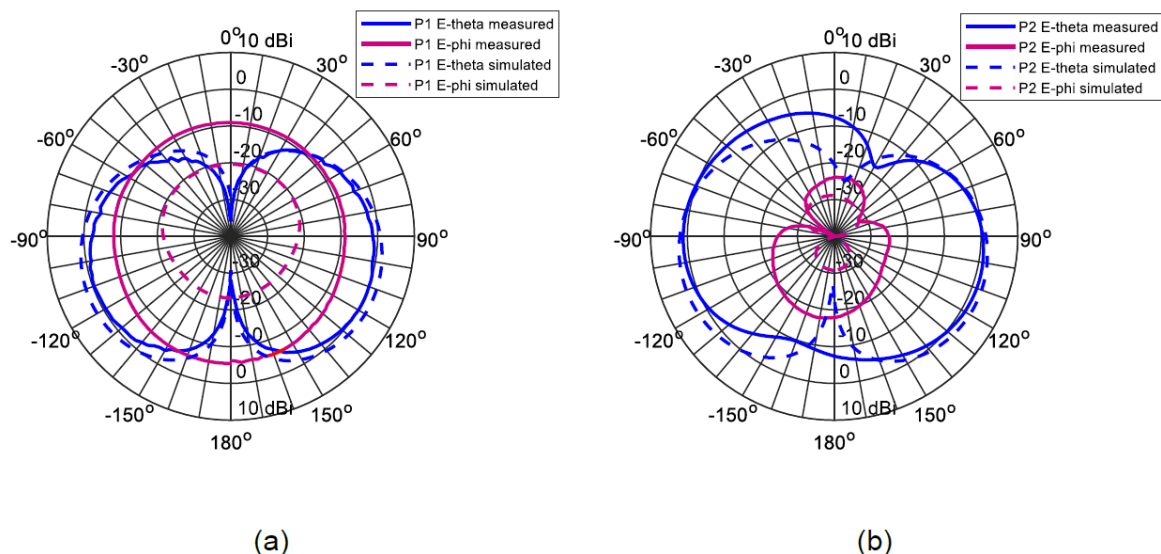
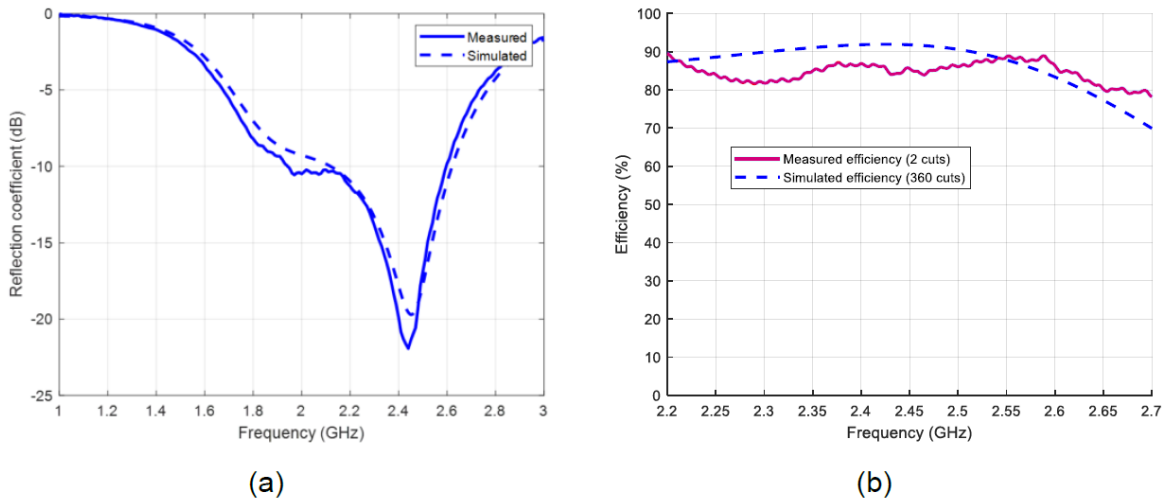


Figure 45. Reflection coefficient (a) and total efficiency (b)

6.2 Inverted-F antenna (IFA)

6.2.1 Printed IFA

The simulated and measured gain patterns of the printed IFA antenna associated with the MB1623 Bluetooth® Low Energy board (Figure 46) are given in Figure 47. Similarly to the three monopole antennas, the short cable connected to the Bluetooth® Low Energy board increases the E_{ϕ} component in the P1 cut and rotates slightly the E_{θ} component in the P2 cut. The maximum measured gain is -0.1 dBi at 2.4 GHz. The measured patterns have been plotted at 2.4 GHz due to a frequency shift on the reflection coefficient.

Figure 48 (a) shows the simulated and measured reflection coefficients. The measurements present a 50 MHz shift compared to the simulation. A retro-simulation of the antenna using a relative permittivity of 4.7 for the substrate fits the measurements. The design is adjusted accordingly. The measured antenna has a reflection coefficient better than -7.5 dB over the Bluetooth® band (From 2.4 to 2.485 GHz) due to the frequency shift. Figure 48 (b) presents the simulated and measured efficiency. The measured efficiency is over-estimated because of the non-revolutionary shape of the E_{θ} pattern in the P1 cut. The minimum measured efficiency is 86 % in the Bluetooth® band.

Figure 46. Printed IFA

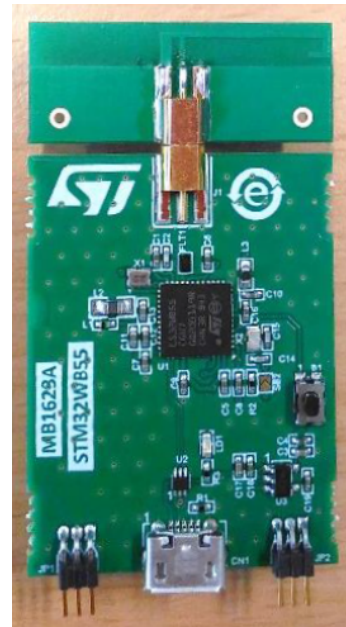


Figure 47. Measured and simulated gain patterns at 2.4 GHz and 2.45 GHz respectively for the P1 (a) and P2 (b) cuts

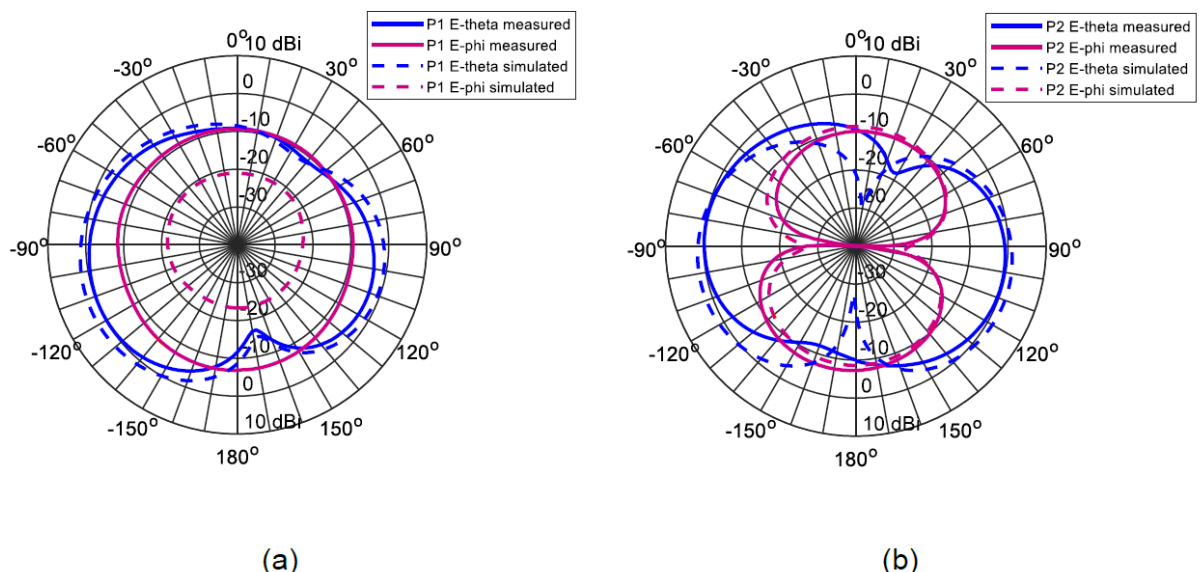
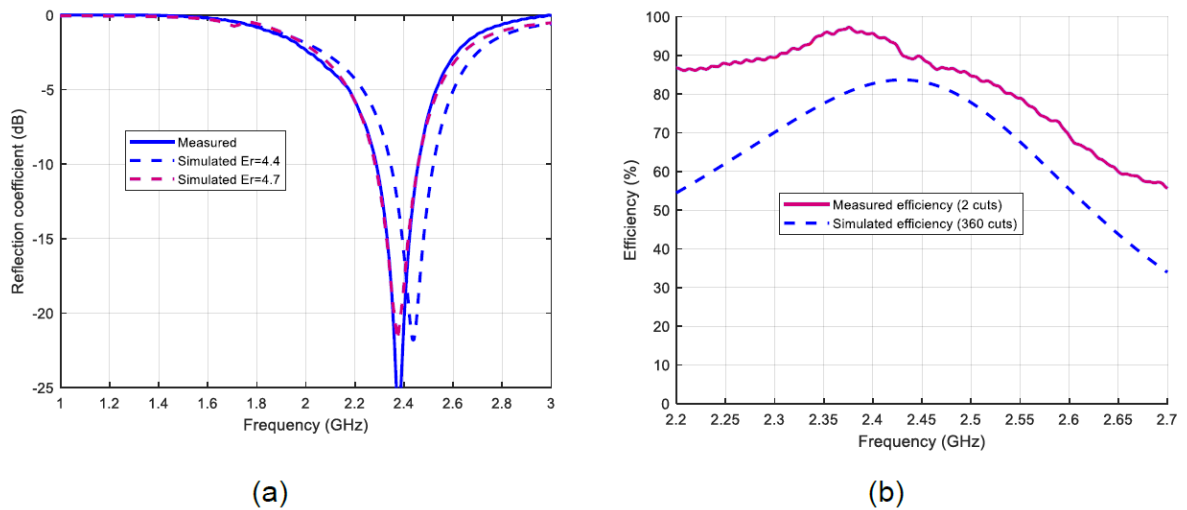


Figure 48. Reflection coefficient (a) and total efficiency (b)

6.2.2 Metallic IFA

The simulated and measured gain patterns of the metallic IFA associated to the MB1623 Bluetooth® Low Energy board (Figure 49) are shown in Figure 50. The results are close, although the measured $E_{\phi i}$ component in the P1 cut is slightly higher than the simulation. The maximum measured gain is 0.0 dBi at 2.4 GHz. The measured patterns have been plotted at 2.4 GHz due to a frequency shift on the reflection coefficient.

Figure 51 (a) shows the simulated and measured reflection coefficients. The measurements present a 50 MHz shift compared to the simulation. A retro-simulation of the antenna using a relative permittivity of 4.7 for the substrate approximates the measurements. The design is adjusted accordingly. The measured antenna has a reflection coefficient better than -6.2 dB over the Bluetooth® band (From 2.4 to 2.485 GHz) due to the frequency shift. Figure 51 (b) presents the simulated and measured efficiency. The minimum measured efficiency is 81 % in the Bluetooth® band.

Figure 49. Metallic IFA

Figure 50. Measured and simulated gain patterns at 2.4 GHz and 2.45 GHz respectively for the P1 (a) and P2 (b) cuts

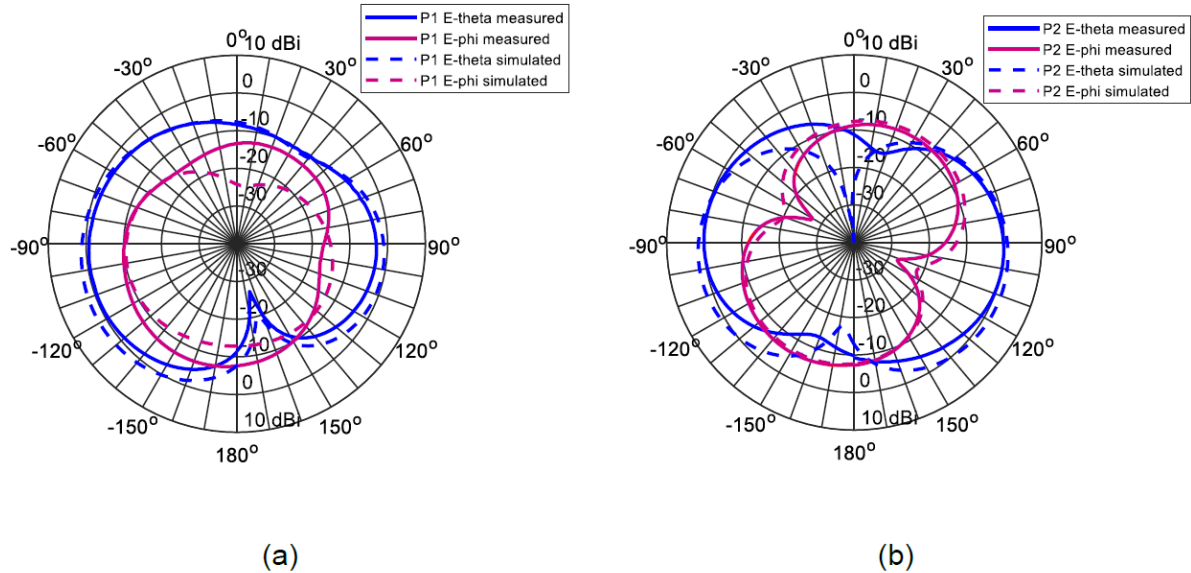
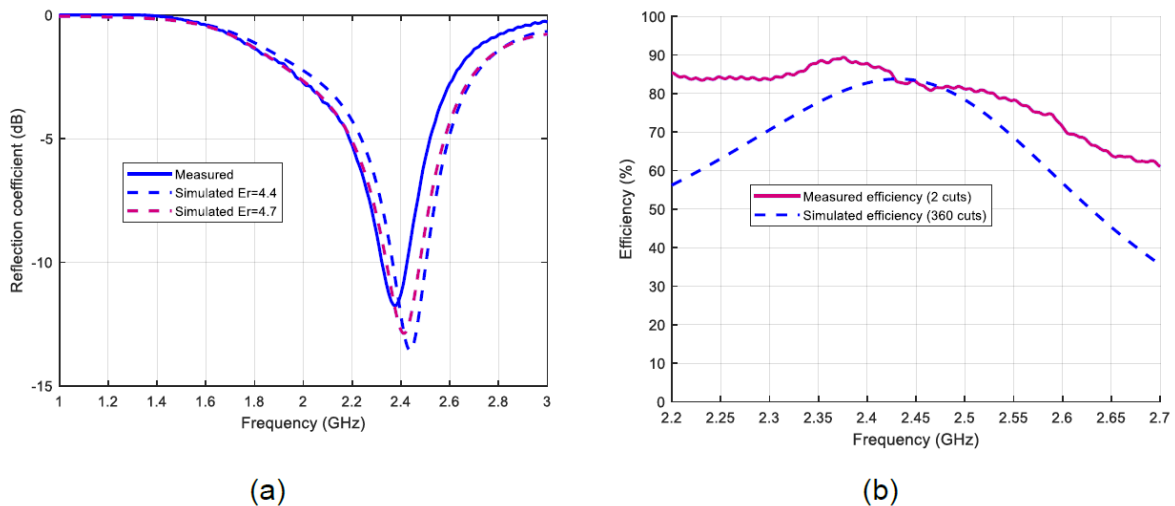


Figure 51. Reflection coefficient (a) and total efficiency (b)



6.3

Yagi-Uda antenna

The simulated and measured gain patterns of the Yagi-Uda antenna connected to the MB1623 Bluetooth® Low Energy board (Figure 52) are plotted in Figure 53. Since the radiation has a lobe in the opposite direction of the Bluetooth® Low Energy board, the patterns are almost not affected by the added short coaxial cable. The maximum measured gain is 5.6 dBi at 2.4 GHz. The measured patterns have been plotted at 2.4 GHz due to a frequency shift on the reflection coefficient.

Figure 54 (a) presents the simulated and measured reflection coefficients. The measurements present a 50 MHz shift compared to the simulation. A retro-simulation of the antenna using a relative permittivity of 4.7 for the substrate overlaps the measured S11. The design will be adjusted accordingly. The measured antenna has a reflection coefficient better than -5.6 dB over the Bluetooth® band (From 2.4 to 2.485 GHz) due to the frequency shift. Figure 54 (b) presents the simulated and measured efficiency. The minimum measured efficiency is 67 % in the Bluetooth® band.

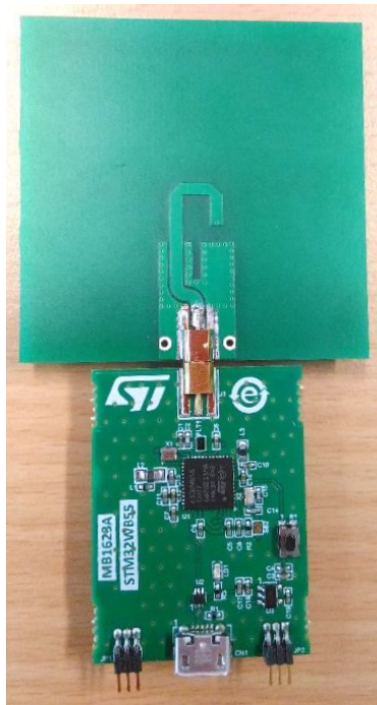
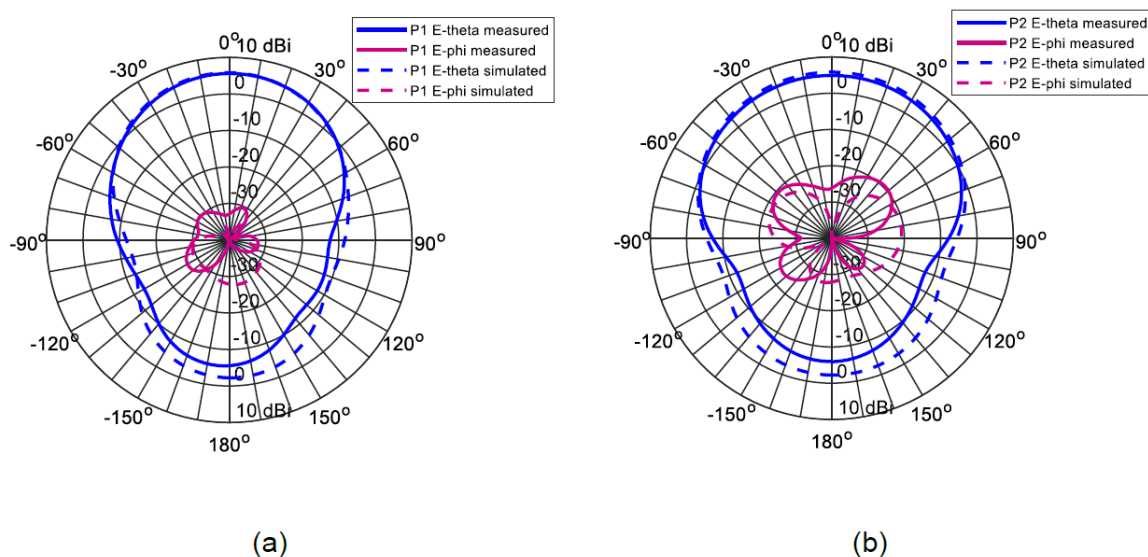
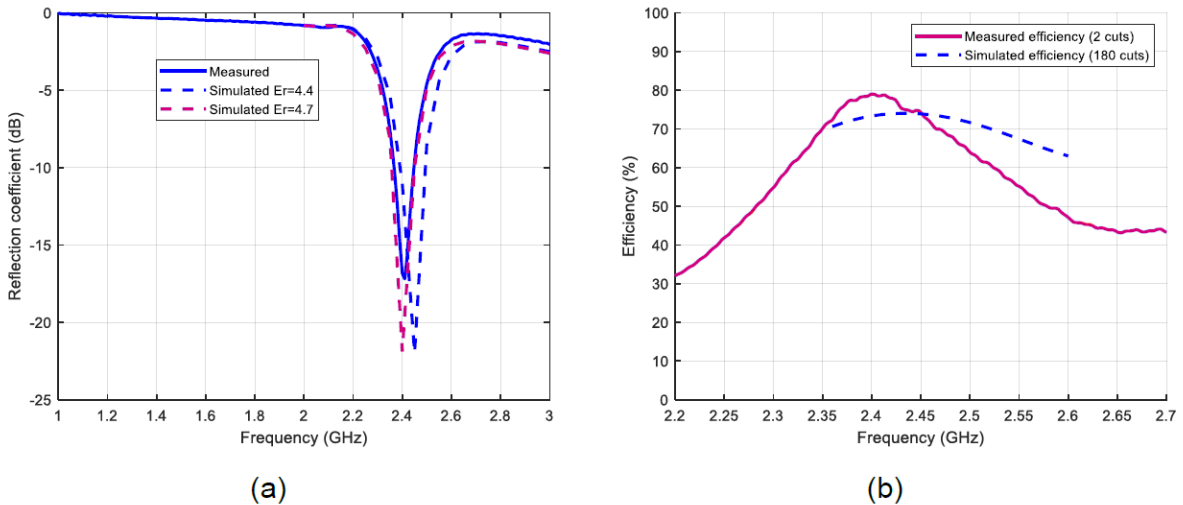
Figure 52. Yagi-Uda antenna**Figure 53.** Measured and simulated gain patterns at 2.4 GHz and 2.45 GHz respectively for the P1 (a) and P2 (b) cuts

Figure 54. Reflection coefficient (a) and total efficiency (b)

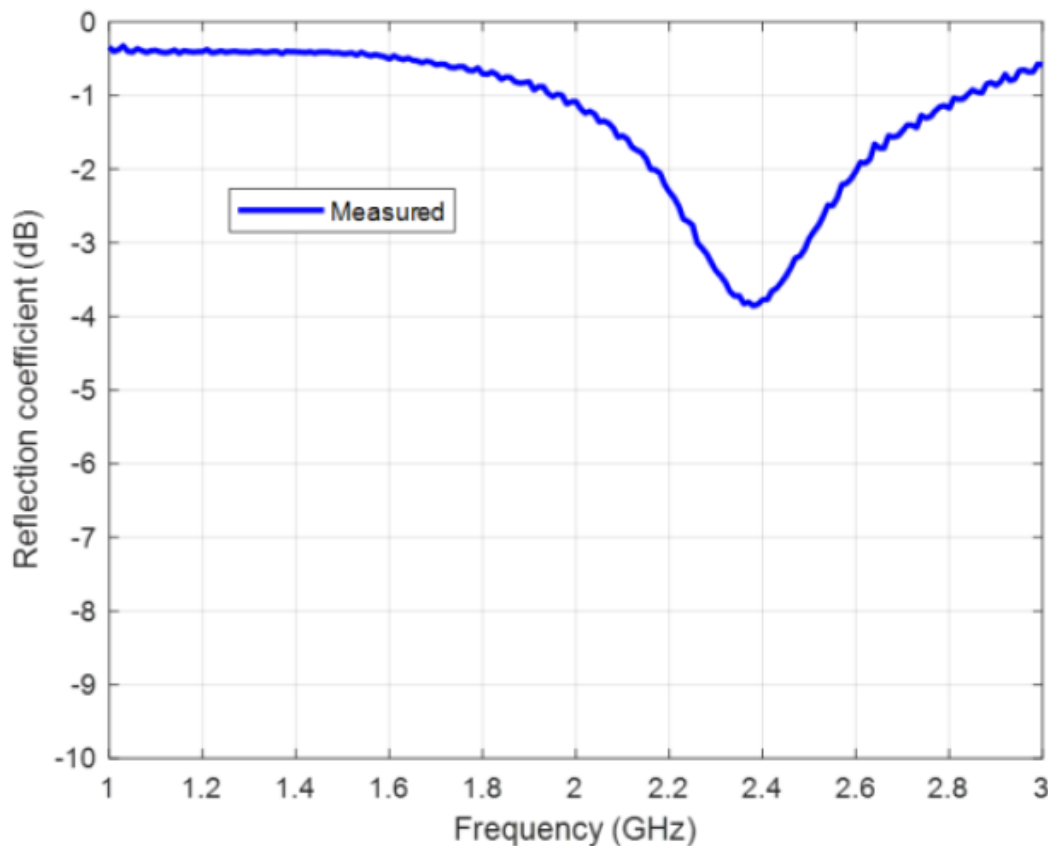
6.4

Reference antenna

The selected reference antenna is the TDK ANT016008LCS2442MA2. The recommended layout is narrow and long ($10 \times 50 \text{ mm}^2$) which is not convenient for the MB1623 Bluetooth® Low Energy board. A $20 \times 30 \text{ mm}^2$ circuit is fabricated (Figure 55) to be consistent with the width of the Bluetooth® Low Energy board and the monopole and IFA antennas. Since the size of the ground plane is different from the recommended one, the components of the matching circuit are different than the ones used in the datasheet. The first step consists in measuring the raw reflection coefficient. Figure 56 presents the measured S11. Based on this result, the matching is carried out. After that, the gain patterns are measured.

Figure 55. Reference antenna

Figure 56. Reflection coefficient



7

Conclusion

Seven antenna designs are carried out taking into account the MB1623 board. Monopole like antennas (T, L and meander shaped) propose very similar radiation properties with wide frequency bandwidth, thanks to the coupling with the chipboard. A similar high radiation efficiency (Superior to 90 %) is obtained for this kind of antenna. The printed and metal IFA show a narrower operating bandwidth and radiation properties close to the dipole antenna, with higher cross-polarization and radiation efficiency of the same order (Superior to 80 %). The Yagi-Uda antenna provides unidirectional radiation with higher gain (~6 dBi) over a limited operation bandwidth. Radiation efficiency is slightly lower (Superior to 70 %) than those of the other antenna topologies.

Overall, the measurements are in agreement with the simulation. Some discrepancies are observed on the gain patterns due to the added short coaxial cable introduced to connect the antenna to the measurement instrument. Some frequency shifts are detectable with a narrow band antenna (Printed IFA, metallic IFA, and Yagi-Uda) designs due to a change in dielectric substrate permittivity. Three antenna designs are retuned with the new value of substrate permittivity for impedance matching improvement over the frequency band of interest. A summary of the measured radio-electrical characteristics based on two cuts is provided in [Table 2](#).

Table 2. Measured radio-electrical characteristics

Antenna type	Maximum gain at 2.45 GHz (dB) ⁽¹⁾	Maximum reflection coefficient (dB)	Minimum efficiency (%)
T-shaped monopole	2.0	-16	90
L-shaped monopole	1.3	-16	94
Meandered monopole	1.3	-18	84
Printed IFA	-0.1	-7.5	86
Metallic IFA	0.0	-6.2	81
Yagi-Uda	5.6	-5.6	67

1. 2.4 GHz for the IFA and Yagi-Uda antennas

8 References

Table 3. References

ID	Description
[1]	W.-S. C. a. K.-L. W. Chih-Ming Su, «Metal-plate shorted T-shaped monopole for internal laptop antenna for 2.4/5 GHz WLAN operation,» IEEE Antennas and Propagation Society Symposium, Monterey, CA, USA, vol. 2, pp. 1943-1946, 2004.
[2]	J.-Y. J. a. L.-C. Tseng, «Planar monopole antennas for 2.4/5.2 GHz dual-band application,» IEEE Antennas and Propagation Society International Symposium. Digest. Held in conjunction with USNC/CNC/URSI North American Radio Sci. Meeting (Cat. No.03CH37450), vol. 4, pp. 158-161, 2003.
[3]	Y.-L. K. a. K.-L. Wong, «Printed double-T monopole antenna for 2.4/5.2 GHz dual-band WLAN operations,» in IEEE Transactions on Antennas and Propagation, vol. 51, n° %19, pp. 2187-2192, Septembre 2003.
[4]	M. K. G. T. a. V. M. Soras, «Analysis and design of an inverted-F antenna printed on a PCMCIA card for the 2.4 GHz ISM band,» IEEE Antennas and Propagation Magazine, vol. 44, n° %11, pp. 37-44, 2002.
[5]	M. Z. A. A. A. M. N. H. a. P. J. S. D. Misman, «Design of planar meander line antenna,» 2009 3rd European Conference on Antennas and Propagation, pp. 2420-2424, 2009.
[6]	R. S. a. J. Y. H. Nakano, «Low-profile inverted-F antenna with parasitic elements on an infinite ground plane,» IEEE Proceedings - Microwaves, Antennas and Propagation, vol. 145, n° %14, pp. 321-325, 1998.
[7]	H. Yagi, «Beam transmission of ultra-short waves,» Proc. IRE, vol. 16, pp. 715-741, 1928.

Revision history

Table 4. Document revision history

Date	Version	Changes
31-Jan-2020	1	Initial release.

Contents

1	Reference board	2
2	Context	3
3	Antenna designs and simulated performances	4
3.1	Used coordinates for gain patterns	4
3.2	Monopole T-shaped antenna	5
3.2.1	Configuration	5
3.2.2	Simulation results	6
3.3	Monopole L-shaped antenna	8
3.3.1	Configuration	8
3.3.2	Simulation results	8
3.4	Meander line antenna	10
3.4.1	Configuration	10
3.4.2	Simulation results	11
3.5	Inverted F antenna - IFA	13
3.5.1	Configuration	13
3.5.2	Simulation results	13
3.6	Metallic inverted F antenna	15
3.6.1	Configuration	15
3.6.2	Simulation results	16
3.7	Yagi-Uda antenna	18
3.7.1	Configuration	18
3.7.2	Simulation results	18
3.8	Chip antenna	20
4	Fabrication of the prototypes	21
5	Measurement setups	22
5.1	Reflection coefficient	22
5.2	Gain patterns	22
5.3	Efficiency	23
5.4	Coordinates for gain patterns	23
5.5	Measurement parameters	23

6	Measurement results	24
6.1	Monopole antennas	24
6.1.1	T-shaped antenna	24
6.1.2	L-shaped antenna	26
6.1.3	Meander-line antenna	27
6.2	Inverted-F antenna (IFA)	29
6.2.1	Printed IFA	29
6.2.2	Metallic IFA	31
6.3	Yagi-Uda antenna	32
6.4	Reference antenna	34
7	Conclusion	36
8	References	37
Revision history		38
Contents		39
List of tables		41
List of figures.....		42

List of tables

Table 1.	Measurement parameters	23
Table 2.	Measured radio-electrical characteristics	36
Table 3.	References	37
Table 4.	Document revision history	38

List of figures

Figure 1.	Reference board	2
Figure 2.	Coordinate system used in simulations for the gain patterns	4
Figure 3.	Monopole T-shaped antenna configuration: (a) simplified model (b) complete model	5
Figure 4.	Simulated return loss versus frequency for simple and complete models	6
Figure 5.	Simulated input impedance versus frequency for simple and complete models	7
Figure 6.	Simulated total efficiency versus frequency for simple and complete models	7
Figure 7.	Simulated radiation pattern for the simplified and complete models at 2.45 GHz: (a) $\varphi=0^\circ$: XZ plane, (b) $\varphi=90^\circ$: YZ plane, (c) $\Theta=90^\circ$: XY plane	8
Figure 8.	Monopole L-shaped antenna configuration: (a) simplified model (b) complete model	8
Figure 9.	Simulated return loss versus frequency for simple and complete models	9
Figure 10.	Simulated Input impedance versus frequency for simple and complete models	9
Figure 11.	Simulated efficiency versus frequency for simple and complete models	10
Figure 12.	Simulated radiation pattern for the simplified and complete models at 2.45 GHz: (a) $\varphi=0^\circ$ (XZ plane), (b) $\varphi=90^\circ$ (YZ plane), (c) $\Theta=90^\circ$ (XY plane)	10
Figure 13.	Meander line antenna configuration: (a) simplified model (b) complete model	11
Figure 14.	Simulated reflection coefficient versus frequency for simple and complete models	11
Figure 15.	Simulated input impedance versus frequency for simple and complete models	12
Figure 16.	Simulated efficiency versus frequency for simple and complete models	12
Figure 17.	Simulated radiation pattern for the simplified and complete models at 2.45 GHz: (a) $\varphi=0^\circ$ (XZ plane), (b) $\varphi=90^\circ$ (YZ plane), (c) $\Theta=90^\circ$ (XY plane)	13
Figure 18.	Inverted-F antenna configuration: (a) simplified model (b) complete model	13
Figure 19.	Simulated return loss versus frequency for simple and complete models	14
Figure 20.	Simulated input impedance versus frequency for simple and complete models	14
Figure 21.	Simulated efficiency versus frequency for simple and complete models	15
Figure 22.	Simulated radiation pattern for the simplified and complete models at 2.45 GHz: (a) $\varphi=0^\circ$ (XZ plane), (b) $\varphi=90^\circ$ (YZ plane), (c) $\Theta=90^\circ$ (XY plane)	15
Figure 23.	Metallic inverted F antenna configuration: (a) simplified model (b) complete model	16
Figure 24.	Simulated return loss versus frequency for simple and complete models	16
Figure 25.	Simulated input impedance versus frequency for simple and complete models	17
Figure 26.	Simulated efficiency versus frequency for simple and complete models	17
Figure 27.	Simulated radiation pattern for the simplified and complete models at 2.45 GHz: (a) $\varphi=0^\circ$ (XZ plane), (b) $\varphi=90^\circ$ (YZ plane), (c) $\Theta=90^\circ$ (XY plane)	18
Figure 28.	Geometry of the Yagi-Uda antenna	18
Figure 29.	Simulated reflection coefficient of the Yagi-Uda antenna	19
Figure 30.	Simulated input impedance of the Yagi-Uda antenna	19
Figure 31.	Simulated efficiency of the Yagi-Uda antenna	20
Figure 32.	Simulated radiation pattern of the Yagi-Uda antenna at 2.45 GHz: (a) $\varphi=0^\circ$ (XoZ plane), (b) $\varphi=90^\circ$: (YoZ plane), (c) $\Theta=90^\circ$: (XoY plane)	20
Figure 33.	Exploded view of the layout	21
Figure 34.	Pictures of the realized PCB (Top layer on the left, and bottom layer on the right)	21
Figure 35.	UHF anechoic chamber configuration for passive antenna measurements	23
Figure 36.	Antenna positioning during measurements	24
Figure 37.	Monopole T-shaped antenna	25
Figure 38.	Gain patterns at 2.45 GHz for the P1 (a) and P2 (b) cuts	25
Figure 39.	Reflection coefficient (a) and total efficiency (b)	26
Figure 40.	Monopole L-shaped antenna	26
Figure 41.	Gain patterns at 2.45 GHz for the P1 (a) and P2 (b) cuts	27
Figure 42.	Reflection coefficient (a) and total efficiency (b)	27
Figure 43.	Monopole meandered antenna	28
Figure 44.	Gain patterns at 2.45 GHz for the P1 (a) and P2 (b) cuts	28
Figure 45.	Reflection coefficient (a) and total efficiency (b)	29
Figure 46.	Printed IFA.	30

Figure 47.	Measured and simulated gain patterns at 2.4 GHz and 2.45 GHz respectively for the P1 (a) and P2 (b) cuts	30
Figure 48.	Reflection coefficient (a) and total efficiency (b).	31
Figure 49.	Metallic IFA	31
Figure 50.	Measured and simulated gain patterns at 2.4 GHz and 2.45 GHz respectively for the P1 (a) and P2 (b) cuts	32
Figure 51.	Reflection coefficient (a) and total efficiency (b).	32
Figure 52.	Yagi-Uda antenna	33
Figure 53.	Measured and simulated gain patterns at 2.4 GHz and 2.45 GHz respectively for the P1 (a) and P2 (b) cuts	33
Figure 54.	Reflection coefficient (a) and total efficiency (b).	34
Figure 55.	Reference antenna	34
Figure 56.	Reflection coefficient	35

IMPORTANT NOTICE – PLEASE READ CAREFULLY

STMicroelectronics NV and its subsidiaries ("ST") reserve the right to make changes, corrections, enhancements, modifications, and improvements to ST products and/or to this document at any time without notice. Purchasers should obtain the latest relevant information on ST products before placing orders. ST products are sold pursuant to ST's terms and conditions of sale in place at the time of order acknowledgement.

Purchasers are solely responsible for the choice, selection, and use of ST products and ST assumes no liability for application assistance or the design of Purchasers' products.

No license, express or implied, to any intellectual property right is granted by ST herein.

Resale of ST products with provisions different from the information set forth herein shall void any warranty granted by ST for such product.

ST and the ST logo are trademarks of ST. For additional information about ST trademarks, please refer to www.st.com/trademarks. All other product or service names are the property of their respective owners.

Information in this document supersedes and replaces information previously supplied in any prior versions of this document.

© 2020 STMicroelectronics – All rights reserved